3DCTRL project

Algorithm Theoretical Basis Document v2.0 | D2

Doc. ID	3DCTRL_ATBD_D2
Issue	1.9
Date	09.05.2024
Prepared by	D. Efremenko, R. Lutz, V. Molina Garcia, S. Seo and A. Doicu (DLR) H. Yu (BIRA)
Status	Initial

Aristotle University of Thessaloniki – Laboratory of Astrophysics | AUTH-LAP
German Aerospace Centre - Remote Sensing Technology Institute | DLR-IMF
Ludwig-Maximilians-University in Munich | LMU
Norwegian Institute for Air Research | NILU
Royal Belgian Institute for Space Aeronomie | BIRA-IASB

3DCTRL | ESA contract number 4000137834/22/I-AG

DOCUMENT APPROVAL RECORD

	Digital signature:
Prepared by: Dmitry Efremenko, Victor Molina Garcia, Sora Seo, Huan Yu and Adrian Doicu	
Checked by: MariLiza Koukouli	Maria-Elissavet Koukouli Digitally signed by Maria-Elissavet Koukouli Date: 2024.06.12 13:11:33 +03'00'

DOCUMENT CHANGE RECORD

Issue	Date	Change
0.9	10.11.2022	First initial version
1.0	27.02.2023	Final version
1.9	09.05.2024	First initial version
2.0		Final version

Table of Contents

LIST OF FIGURES

LIST OF TABLES

1. Theoretical treatise on retrieval algorithms for 3D cloudy scenes

Trace gas retrievals from nadir-sounding instruments are compromised by the presence of clouds. There are three different cloud effects that affect trace gas retrievals:

1. the albedo effect, related to the enhancement of reflectivity compared to clear scenes,
2. the cloud shadow when a part of the trace gas column is hidden by clouds, and
3. the increase in absorption due to multiple scattering inside clouds.

Most retrieval algorithms are based on the so-called linear mixing model, which is the most important application of the independent column approximation (ICA) to homogeneous broken clouds. In the linear mixing procedure,

1. the radiance of a partly cloudy scene is assumed to be a linear combination of a cloudy and a clear-sky radiance weighted by the cloud fraction, and
2. the cloudy-sky radiance is computed under the assumption that the clouds within each pixel are plane-parallel and homogeneous in horizontal and vertical directions (the ICA approximation).

Although the method is computationally efficient, the errors due to three-dimensional effects can be large, especially for cloudy scenes of small horizontal extent. As the new generation of European atmospheric composition sensors, such as Sentinel 5 Precursor, Sentinel 4 and Sentinel 5, have a high spatial resolution of about 3.5×5.5 km^2 at nadir, fast and more accurate retrieval algorithms, accounting for cloud inhomogeneities, are needed.

In general, a retrieval algorithm consists of a radiative transfer and an inverse model (Figure 1). In particular,

1. a radiative transfer model is used to computed the synthetic radiances $\mathbf{y}$ for a set of retrieval parameters encapsulated in the state vector $\mathbf{x}$, while
2. an inverse model is used to formulate an optimization problem for the synthetic and measured radiances $\mathbf{y}$ and $\mathbf{y}_{\text{mes}}$, respectively.

The optimization problem, consisting in the minimization of some cost function $\mathrm{F}(\mathbf{x})$, is then solved by means of an inversion method (regularization method).

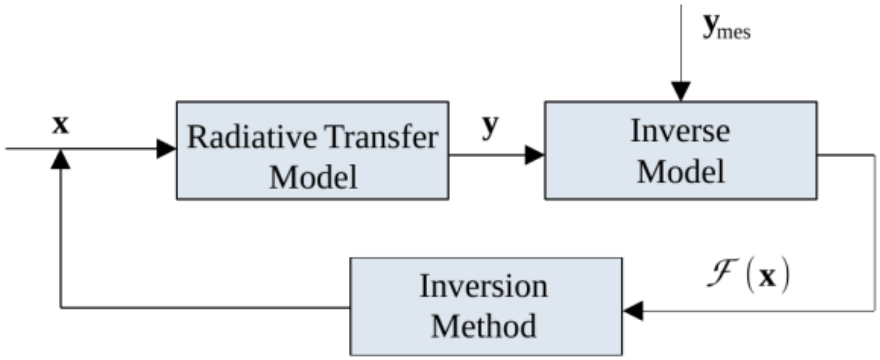

Figure 1. Retrieval algorithm.

This section provides a description of the radiative transfer and inverse models, which are the cornerstones of retrieval algorithms for three-dimensional cloudy scenes.

1.1 Radiative transfer models

In a three-dimensional domain, the radiative transfer equation for the diffuse radiance at point $\mathbf{r}$ in direction $\boldsymbol{\Omega}$ is given by

$$\frac{dI(\mathbf{r},\mathbf{\Omega})}{ds} = -\sigma_{\text{ext}}(\mathbf{r})I(\mathbf{r},\mathbf{\Omega}) + \frac{\sigma_{\text{sct}}(\mathbf{r})}{4\pi}\frac{F_0}{|\mu_0|}P(\mathbf{r},\mathbf{\Omega},\mathbf{\Omega}_0)T(\mathbf{r}_0,\mathbf{r}) + \frac{\sigma_{\text{sct}}(\mathbf{r})}{4\pi}\int_\Omega P(\mathbf{r},\mathbf{\Omega},\mathbf{\Omega}')I(\mathbf{r},\mathbf{\Omega}')\mathrm{d}\mathbf{\Omega}', \quad (1)$$

where

$$T(\mathbf{r}_0,\mathbf{r}) = \exp(-\int_{\mathbf{r}_0}^{\mathbf{r}}\sigma_{\text{ext}}(\mathbf{r}')\mathrm{d}s') \quad (2)$$

is the transmission along the solar direction $\mathbf{\Omega}_0 = (\mu_0,\varphi_0) = (\mathbf{r}-\mathbf{r}_0)/|\mathbf{r}-\mathbf{r}_0|$ with $\mu_0 < 0$, starting at the top-of-atmosphere point $\mathbf{r}_0$ and ending at the field point $\mathbf{r}$, σ_{ext} and $\sigma_{\text{sct}} = \omega\sigma_{\text{ext}}$ are the extinction and scattering coefficients, respectively, ω is the single-scattering albedo, P the phase function, F_0 the solar flux, and Ω the unit sphere. Here, the dependency of the radiance I on the wavelength λ is omitted. For a three-dimensional domain in the shape of rectangular prism with lengths L_{x}, L_{y} and L_{z}, top and bottom faces S_{t} and S_{b}, respectively, and lateral faces $S_{1\text{x}}$ ($x=0$), $S_{2\text{x}}$ ($x=L_{\text{x}}$), $S_{1\text{y}}$ ($y=0$), and $S_{2\text{y}}$ ($y=L_{\text{y}}$), the boundary conditions associated to the radiative transfer equation are (i) homogeneous boundary conditions at the top face S_{t}, (ii) reflective boundary conditions at the bottom face S_{b}, and (iii) periodic boundary conditions at the lateral faces $S_{1\alpha}$ and $S_{2\alpha}$ with $\alpha = \text{x,y}$.

Under the assumption that the distance from the top of the domain to the instrument is large and the instrument footprint is a rectangle with halflengths l_{x} and l_{y}, center coordinates (x_0,y_0), and area $A_{\text{tm}} = 4l_{\text{x}}l_{\text{y}}$, the signal measured by the instrument, that collects the radiances around the direction $\mathbf{\Omega}_{\text{m}}$, is computed as

$$\text{I}(\mathbf{\Omega}_{\text{m}}) = \frac{1}{A_{\text{tm}}}\int_{x_0-l_{\text{x}}}^{x_0+l_{\text{x}}}\int_{y_0-l_{\text{y}}}^{y_0+l_{\text{y}}} I(x,y,\mathbf{\Omega}_{\text{m}})\mathrm{d}x\mathrm{d}y, \quad (3)$$

where $I(x,y,\mathbf{\Omega}_{\text{m}})$ is the radiance at the top-of-domain point $(x,y)\in S_{\text{t}}$ in direction $\mathbf{\Omega}_{\text{m}}$.

Radiative transfer models for three-dimensional cloudy scenes can be either

1. three-dimensional radiative transfer models, and
2. one- and two-dimensional radiative transfer models, which accounts on the three-dimensional cloud effects in an approximate manner.

These are summarized below.

1.1.1 Three-dimensional radiative transfer models

One of the most efficient and widely used multi-dimensional deterministic method in the atmospheric sciences is the Spherical Harmonics Discrete Ordinate Method (SHDOM) developed by Evans [1]. The radiative transfer equation (RTE) is solved in the three-dimensional geometry iteratively by using the spherical harmonic and the discrete ordinate representations of the radiance field. The method combines the spherical harmonic and the discrete ordinate representation of the radiance field. The streaming of the radiation is accurately modeled in the discrete ordinate space, while the computation of the scattering integral is efficiently performed in the spherical harmonic space. Moreover, storing the source function as a spherical harmonic series at each grid point requires less computer memory as compared with a purely discrete ordinate method. The so-called adaptive grid technique improves the solution accuracy by increasing the spatial resolution in regions where the source function is changing more rapidly.

1.1.2 Approximate one-dimensional radiative transfer models

Three-dimensional cloud effects are considered in several one-dimensional radiative transfer models such as, the tilted independent column approximation (TICA), the nonlocal tilted independent column approximation (NTICA), and stochastic radiative transfer models.

1. The tilted independent column approximation (TICA) accounts for the slant incidence of the sun. Specifically, either the direct radiation is calculated in a single, independent column that is slanted toward the sun and the diffuse radiation is calculated in the vertical column [2], or both the direct and diffuse radiations are calculated in the tilted, independent columns that are slanted according to the solar zenith and azimuth angles [3].

2. The nonlocal tilted independent column approximation (NTICA) accounts for the diffuse radiation transport between the tilted columns. Specifically, the scattering into neighboring columns is taken into account by convolving the ICA and TICA reflectances with a gamma [4] and a Gaussian [5] kernel, respectively. A relatively recent version of TICA is the parameterized NTICA (paNTICA), in which the convolution is carried out with a parameterized kernel that is suitable for different model resolutions and cloud scenes [6].

3. Stochastic radiative transfer models consider the cloud fields as stochastic scattering media due to their internal inhomogeneity and stochastic geometry. Representing the extinction field σ_{ext} and the radiance field I as the sum of their mean values $\langle\sigma_{\text{ext}}\rangle$ and $\langle I\rangle$, and their random fluctuations σ'_{ext} and I', that is, $\sigma_{\text{ext}}=\langle\sigma_{\text{ext}}\rangle+\sigma'_{\text{ext}}$ and $I=\langle I\rangle+I'$, and by applying the procedure of statistical averaging, an infinite system of equations for the mean value of the radiance field $\langle I\rangle$ and the covariances of the fluctuations of the extinction and radiance fields $\langle\sigma'^{n}_{\text{ext}}I'\rangle$, $n\geq 1$ can be derived [7]. This system of equations is truncated at a certain stage, and then closed by applying an independent hypothesis on the higher-order covariance terms $\langle\sigma'^{(n+1)}_{\text{ext}}I'\rangle$. A zeroth-order stochastic model consists of an one-dimensional radiative transfer equation for $\langle I\rangle$, in which the closure relations $\langle\sigma'_{\text{ext}}I'\rangle=0$ and $\langle\sigma'_{\text{ext}}I'\rangle=C\langle\sigma_{\text{ext}}\rangle\langle I\rangle$ with C being a normalization constant, were considered in Refs. [2] and [8], respectively. Note that for broken clouds, the identity $\langle\sigma'^{2}_{\text{ext}}I'\rangle=(1-\langle\sigma_{\text{ext}}\rangle)\langle\sigma'_{\text{ext}}I'\rangle$ implies that the n th-order stochastic model reduces to a first-order stochastic model consisting of an one-dimensional radiative transfer equation for a two-dimensional radiance vector with entries $\langle I\rangle$ and $\langle\sigma'_{\text{ext}}I'\rangle$ [7].

1.1.3 Approximate two-dimensional radiative transfer models

Modeling the radiative transfer in a two-dimensional plane, say the xz -plane, assumes that

1. the optical properties depend on x and z, and not on y, and

2. the solar direction $\boldsymbol{\Omega}_0$ is in the xz -plane.

These assumptions show that a three-dimensional radiative transfer is not equivalent with a two-dimensional radiative transfer. For this reason and a correct modeling, a two-dimensional radiative transfer model should take into account in a certain way the three-dimensional effects. This is the role of approximate two-dimensional radiative transfer models. While approximate one-dimensional radiative transfer models try to reduce the 3D-to-1D errors, approximate two-dimensional radiative transfer models try to reduce the 3D-to-2D errors. Because in a three-dimensional geometry, a two-dimensional model reproduces more accurately the transport of radiation than a one-dimensional model, the first ones are more accurate but less efficient.

For this project, approximate two-dimensional radiative transfer models were designed. The first two models, are an extension of the independent column approximation to a two-dimensional geometry, discussed in 1.1.3.1, while the third one is a stochastic model involving an averaging operator with respect to one horizontal coordinate (i.e., the y -coordinate), discussed in 1.1.3.2. Because these models are new, they are presented here in detail [9].

1.1.3.1 Independent slice approximation

Assume that the solar direction is in the xz plane (the solar azimuth angle is 0) and let $I_{3D}(x,y,z,\mathbf{\Omega})$ be the radiance computed by a three-dimensional radiative transfer model, $I_{2D}(x,z,\mathbf{\Omega}\,|\,y)$ the radiance computed by a two-dimensional model in a plane y, $I_{2D}(x,\mathbf{\Omega}_{\rm m}\,|\,y)$ the radiance at point $x\in S_{\rm t}$ in direction $\mathbf{\Omega}_{\rm m}$, and

$$\mathrm{I}_{2D}(\mathbf{\Omega}_{\rm m}\,|\,y)=\frac{1}{2l_{\rm x}}\int_{x_0-l_{\rm x}}^{x_0+l_{\rm x}}I_{2D}(x,\mathbf{\Omega}_{\rm m}\,|\,y)\mathrm{d}x, \tag{4}$$

the signal measured by an one-dimensional detector in the xz-plane.

The transport of radiation along the y-axis can be taken into account by representing the top-of-domain radiance $I_{3D}(x,y,\mathbf{\Omega}_{\rm m})$ as

$$I_{3D}(x,y,\mathbf{\Omega}_{\rm m})=\int_{y_0-\ell}^{y_0+\ell}K(y'-y)I_{2D}(x,\mathbf{\Omega}_{\rm m}\,|\,y')\mathrm{d}y', \tag{5}$$

where $K(y'-y)$ is a smoothing kernel and 2ℓ the length of the kernel. Inserting Eq. (5) in Eq. (3), and taking Eq. (4) into account, we obtain

$$\mathrm{I}_{3D}(\mathbf{\Omega}_{\rm m})=\frac{1}{2l_{\rm y}}\int_{y_0-l_{\rm y}}^{y_0+l_{\rm y}}\left[\int_{y_0-\ell}^{y_0+\ell}K(y'-y)\mathrm{I}_{2D}(\mathbf{\Omega}_{\rm m}\,|\,y')\mathrm{d}y'\right]\mathrm{d}y. \tag{6}$$

Different convolution kernels can be used, as for example, the Gaussian distribution $K(y'-y)=C\exp[-(y'-y)^2/(2\sigma^2)]$, where C is a constant obtained from the normalization condition $\int_{y_0-\ell}^{y_0+\ell}K(y'-y)\mathrm{d}y'=1$. In the parameterized nonlocal tilted independent column approximation (paNTICA)[6], it was found that a good choice for the standard deviation σ of the Gaussian distribution is $\sigma=f(d_{\rm cb}/|\mu_0|)$, where $d_{\rm cb}$ is the distance from the center of the surface pixel to the center of the base of the closest cloud, and f is a parameter that depends on the cloud scene and ranges between 0.5 and 1.5. However, when an optimal value or an appropriate parameterization for σ are not available, we may choose K as

1. the uniform distribution

$$K(y'-y)=K(y'-y_0)=\begin{cases}\dfrac{1}{2\ell}, & y_0-\ell\le y'\le y_0+\ell\\ 0, & \text{otherwise}\end{cases}, \tag{7}$$

yielding the y-averaging formula

$$\mathrm{I}_{3D}(\mathbf{\Omega}_{\rm m})=\frac{1}{2\ell}\int_{y_0-\ell}^{y_0+\ell}\mathrm{I}_{2D}(\mathbf{\Omega}_{\rm m}\,|\,y)\mathrm{d}y, \tag{8}$$

or

2. the Dirac delta distribution ($\ell\to\infty$) $K(y'-y)=K(y'-y_0)=\delta(y'-y_0)$, yielding the y-center-point formula

$$\mathrm{I}_{3D}(\mathbf{\Omega}_{\rm m})=\mathrm{I}_{2D}(\mathbf{\Omega}_{\rm m}\,|\,y_0). \tag{9}$$

In the following, the models relying on the y-averaging formula (6) and the y-center-point formula (9) will be referred to as the nonlocal independent slice approximation (NISA), and simply, the independent slice approximation (ISA), respectively. As compared to NISA, ISA does not take into account the transport of radiation along the y-axis but is more efficient (since it requires the solution of only one two-dimensional radiative transfer problem).

1.1.3.2 Stochastic model

In stochastic models, the ensemble-averaging operator $\langle\cdot\rangle$ is interpreted as a domain-averaging operator. Applying the domain-averaging operator with respect to the y coordinate $\langle\cdot\rangle_y$ to Eq. (1), where $\langle f\rangle_y = (1/L_y)\int_0^{L_y} f(x,y,z)\mathrm{d}y$, leads to a radiative transfer equation in which $\mathrm{d}\langle I\rangle_y/\mathrm{d}s$ is expressed in terms of $\langle\sigma_{\mathrm{ext}}I\rangle_y$ and $\langle\sigma_{\mathrm{sct}}PI\rangle_y$. The zeroth-order closure approximation is to set $\langle\sigma_{\mathrm{ext}}I\rangle_y = \langle\sigma_{\mathrm{ext}}\rangle_y\langle I\rangle_y$ and $\langle\sigma_{\mathrm{sct}}PI\rangle_y = \langle\sigma_{\mathrm{sct}}P\rangle_y\langle I\rangle_y$, yielding

$$\begin{aligned}\frac{\mathrm{d}\langle I(\mathbf{r},\boldsymbol{\Omega})\rangle_y}{\mathrm{d}s} &= -\langle\sigma_{\mathrm{ext}}(\mathbf{r})\rangle_y\langle I(\mathbf{r},\boldsymbol{\Omega})\rangle_y + \frac{1}{4\pi}\frac{F_0}{|\mu_0|}\langle\sigma_{\mathrm{sct}}(\mathbf{r})P(\mathbf{r},\boldsymbol{\Omega},\boldsymbol{\Omega}_0)T(\mathbf{r}_0,\mathbf{r})\rangle_y \\ &+\frac{1}{4\pi}\int_\Omega\langle\sigma_{\mathrm{sct}}(\mathbf{r})P(\mathbf{r},\boldsymbol{\Omega},\boldsymbol{\Omega}')\rangle_y\langle I(\mathbf{r},\boldsymbol{\Omega}')\rangle_y\mathrm{d}\boldsymbol{\Omega}'.\end{aligned} \tag{10}$$

Note that the closure relation $\langle\sigma_{\mathrm{ext}}I\rangle_y = \langle\sigma_{\mathrm{ext}}\rangle_y\langle I\rangle_y$ is equivalent with the closure relation $\langle\sigma'_{\mathrm{ext}}I'\rangle_y = 0$, where σ'_{ext} and I' are the fluctuating parts of σ_{ext} and I, respectively. For a practical implementation of Eq. (10), we have two options depending on whether the phase function P depends on the position or not.

Option 1. When the phase function depends on position, i.e., $P = P(\mathbf{r},\boldsymbol{\Omega},\boldsymbol{\Omega}')$, the product $\langle\sigma_{\mathrm{sct}}P\rangle_y$ is computed as

$$\langle\sigma_{\mathrm{sct}}(\mathbf{r})P(\mathbf{r},\boldsymbol{\Omega},\boldsymbol{\Omega}')\rangle_y = \langle\sigma_{\mathrm{sct}}(\mathbf{r})\rangle_y\langle P(\mathbf{r},\boldsymbol{\Omega},\boldsymbol{\Omega}')\rangle_y, \tag{11}$$

where for $P(\mathbf{r},\boldsymbol{\Omega},\boldsymbol{\Omega}') = P(\mathbf{r},\boldsymbol{\Omega}\cdot\boldsymbol{\Omega}') = \sum_{n=1}^{N_{\mathrm{rank}}}\chi_n(\mathbf{r})P_n(\boldsymbol{\Omega}\cdot\boldsymbol{\Omega}')$, the y-average phase function $\langle P\rangle_y$ is given by

$$\langle P(\mathbf{r},\boldsymbol{\Omega},\boldsymbol{\Omega}')\rangle_y = \sum_{n=1}^{N_{\mathrm{rank}}}\left[\frac{\langle\sigma_{\mathrm{sct}}(\mathbf{r})\chi_n(\mathbf{r})\rangle_y}{\langle\sigma_{\mathrm{sct}}(\mathbf{r})\rangle_y}\right]P_n(\boldsymbol{\Omega}\cdot\boldsymbol{\Omega}'), \tag{12}$$

with $P_n(\boldsymbol{\Omega}\cdot\boldsymbol{\Omega}') = P_n(\cos\Theta)$ being the Legendre polynomials, $\chi_n(\mathbf{r})$ the Legendre phase function coefficients, and N_{rank} the maximum expansion order of the phase function. For the product $\langle\sigma_{\mathrm{sct}}PT\rangle_y$ in Eq. (10), we use the average rule

$$\langle\sigma_{\mathrm{sct}}(\mathbf{r})P(\mathbf{r},\boldsymbol{\Omega},\boldsymbol{\Omega}_0)T(\mathbf{r}_0,\mathbf{r})\rangle_y = \langle\sigma_{\mathrm{sct}}(\mathbf{r})P(\mathbf{r},\boldsymbol{\Omega},\boldsymbol{\Omega}_0)\rangle_y\langle T(\mathbf{r}_0,\mathbf{r})\rangle_y, \tag{13}$$

and obtain

$$\begin{aligned}\frac{\mathrm{d}\langle I(\mathbf{r},\boldsymbol{\Omega})\rangle_y}{\mathrm{d}s} &= -\langle\sigma_{\mathrm{ext}}(\mathbf{r})\rangle_y\langle I(\mathbf{r},\boldsymbol{\Omega})\rangle_y + \frac{\langle\sigma_{\mathrm{sct}}(\mathbf{r})\rangle_y}{4\pi}\frac{F_0}{|\mu_0|}\langle P(\mathbf{r},\boldsymbol{\Omega},\boldsymbol{\Omega}_0)\rangle_y\langle T(\mathbf{r}_0,\mathbf{r})\rangle_y \\ &+\frac{\langle\sigma_{\mathrm{sct}}(\mathbf{r})\rangle_y}{4\pi}\int_\Omega\langle P(\mathbf{r},\boldsymbol{\Omega},\boldsymbol{\Omega}')\rangle_y\langle I(\mathbf{r},\boldsymbol{\Omega}')\rangle_y\mathrm{d}\boldsymbol{\Omega}'.\end{aligned} \tag{14}$$

Option 2. When the phase function does not depend on position, i.e., $P = P(\boldsymbol{\Omega},\boldsymbol{\Omega}')$, we have $\left\langle\sigma_{\mathrm{sct}}(\mathbf{r})P(\boldsymbol{\Omega},\boldsymbol{\Omega}')\right\rangle_y = P(\boldsymbol{\Omega},\boldsymbol{\Omega}')\left\langle\sigma_{\mathrm{sct}}(\mathbf{r})\right\rangle_y$ and $\left\langle\sigma_{\mathrm{sct}}(\mathbf{r})P(\boldsymbol{\Omega},\boldsymbol{\Omega}_0)T(\mathbf{r}_0,\mathbf{r}_1)\right\rangle_y = P(\boldsymbol{\Omega},\boldsymbol{\Omega}_0)\left\langle\sigma_{\mathrm{sct}}(\mathbf{r})T(\mathbf{r}_0,\mathbf{r}_1)\right\rangle_y$, in which case, the domain-average equation reads as [2]

$$\begin{aligned}\frac{\mathrm{d}\langle I(\mathbf{r},\boldsymbol{\Omega})\rangle_y}{\mathrm{d}s} &= -\langle\sigma_{\mathrm{ext}}(\mathbf{r})\rangle_y\langle I(\mathbf{r},\boldsymbol{\Omega})\rangle_y + \frac{\langle\sigma_{\mathrm{sct}}(\mathbf{r})\rangle_y}{4\pi}\frac{F_0}{|\mu_0|}P(\boldsymbol{\Omega},\boldsymbol{\Omega}_0)\left[\frac{\langle\sigma_{\mathrm{sct}}(\mathbf{r})T(\mathbf{r}_0,\mathbf{r})\rangle_y}{\langle\sigma_{\mathrm{sct}}(\mathbf{r})\rangle_y}\right] \\ &+\frac{\langle\sigma_{\mathrm{sct}}(\mathbf{r})\rangle_y}{4\pi}\int_\Omega P(\boldsymbol{\Omega},\boldsymbol{\Omega}')\langle I(\mathbf{r},\boldsymbol{\Omega}')\rangle_y\mathrm{d}\boldsymbol{\Omega}'.\end{aligned} \tag{15}$$

In conclusion, the y-average radiance $I_{2\mathrm{D}}(x,z,\boldsymbol{\Omega}) = \langle I(\mathbf{r},\boldsymbol{\Omega})\rangle_y$ solves the radiative transfer equation (14) in the plane xz with the y-average optical parameters $\langle\sigma_{\mathrm{ext}}(\mathbf{r})\rangle_y$, $\langle\sigma_{\mathrm{sct}}(\mathbf{r})\rangle_y$, and $\langle P(\mathbf{r},\boldsymbol{\Omega},\boldsymbol{\Omega}')\rangle_y$. If

$I_{2D}(x,\mathbf{\Omega}_m)$ is the radiance at a top-of-domain point $x \in S_t$ in direction $\mathbf{\Omega}_m$, then the y-average signal measured by the detector is given by $I_{3D}(\mathbf{\Omega}_m) = (1/2l_x)\int_{x_0-l_x}^{x_0+l_x} I_{2D}(x,\mathbf{\Omega}_m)\mathrm{d}x$.

It should be pointed out that the nonlocal independent slice approximation with the choice $\ell = L_y/2$, yielding $I_{3D}(\mathbf{\Omega}_m) = (1/L_y)\int_0^{L_y} I_{2D}(\mathbf{\Omega}_m \mid y)\mathrm{d}y = \langle I_{2D}(\mathbf{\Omega}_m \mid y)\rangle_y$, is similar to the zeroth-order stochastic model. The difference between them consists of which step the y-averaging operator is applied; in the first case, the operator is applied in the last stage on the "two-dimensional" signals, while in the second case, the operator is applied in the first stage on the optical properties of the medium.

1.2 Inverse models

In the case of an atmosphere consisting of gas molecules and a cloud, we assume that
1. the optical coefficients of the gas molecules depend on the altitude level and the wavelength, and
2. the optical coefficients of the cloud depend on the spatial coordinates but not on the wavelength.

The second assumption is justified by the fact that a narrow spectral interval is considered in the retrieval. For N_g gases, the extinction coefficient is computed as

$$\sigma_{\text{ext}}(\lambda,\mathbf{r}) = \sigma_{\text{ext}}^{\text{cloud}}(\mathbf{r}) + \sigma_{\text{sct}}^{\text{mol}}(\lambda,z) + \sum_{g=1}^{N_{\text{g}}} \sigma_{\text{absg}}^{\text{gas}}(\lambda,z), \tag{16}$$

where $\sigma_{\text{ext}}^{\text{cloud}}(\mathbf{r})$ is the extinction coefficient in the cloud, $\sigma_{\text{sct}}^{\text{mol}}(\lambda,z)$ the molecular scattering coefficient due to Rayleigh scattering, $\sigma_{\text{absg}}^{\text{gas}}(\lambda,z)$ the absorption coefficient of gas g, and (x,y,z) the Cartesian coordinates of point $\mathbf{r}$. Considering a discretization of the atmosphere in N_{z} levels, i.e., $\{z_j\}_{j=1}^{N_{\text{z}}}$, the absorption coefficient on level z_j is given by

$$\sigma_{\text{absg}}^{\text{gas}}(\lambda,z_j) = C_{\text{absg}}(\lambda,z_j) n_g(z_j), \tag{17}$$

where $C_{\text{absg}}(\lambda,z_j)$ and $n_g(z_j)$ are the absorption cross section and the number density of gas j on level z_j, respectively. Under the assumption that on a layer j bounded below by z_j and above by z_{j+1}, the number density $n_g(z)$ varies linearly with respect to z, the partial and total column of gas g are defined, respectively, by

$$x_{g,j} = \int_{z_j}^{z_{j+1}} n_g(z)\mathrm{d}z \approx \frac{\Delta z_j}{2}[n_g(z_j) + n_g(z_{j+1})] \tag{18}$$

and

$$X_g = \int_{z_1}^{z_{N_z}} n_g(z)\mathrm{d}z = \sum_{j=1}^{N_z-1} x_{g,j}, \tag{19}$$

where $\Delta z_j = z_{j+1} - z_j$. The most frequently used inversion models are the differential radiance models and the Differential Optical Absorption Spectroscopy (DOAS) model. These are summarized below.

1.2.1 Differential Radiance Models

As inverse models, two differential radiance models are considered [10]. In the first model, called Differential Radiance Model with Internal smoothing (DRMI), the measured and simulated differential spectra are fitted, while in the second model, called Differential Radiance Model with External smoothing (DRME), the measured differential spectrum is fitted with a simulated spectrum and an added smooth component. The differential models are essentially based on the radiance model (here, the dependency on λ is indicated explicitly, but the dependency on $\mathbf{\Omega}_{\text{m}}$ is omitted)

$$\ln \mathrm{I}_{\text{mes}}^{\delta}(\lambda_k) = \ln \mathrm{I}_{\text{sim}}(\lambda_k,\mathbf{X}) + \sum_{j=1}^{N_{\text{s}}} b_j S_j(\lambda_k,\mathbf{X}_{\text{a}}),\ k = 1,\ldots,N_\lambda, \tag{20}$$

where $\mathbf{X} = [X_1,\ldots,X_{N_{\text{g}}}]$ is the state vector encapsulating the total columns of trace gases, $\mathbf{X}_{\text{a}}$ an a priori state vector, $\mathrm{I}_{\text{mes}}^{\delta}(\lambda_k)$ the signal measured by the instrument at wavelength λ_k, N_λ the number of measurement wavelengths, $\mathrm{I}_{\text{sim}}(\lambda_k,\mathbf{X})$ the signal computed by a multi-dimensional radiative transfer model, $S_j(\lambda_k,\mathbf{X}_{\text{a}})$, the correction spectra describing different kinds of instrumental effects and complex physical phenomena, such as, polarization correction spectrum, undersampling spectrum, offset correction

spectrum, and Ring spectrum, N_s the number of correction spectra, and finally, the wavelength independent coefficients b_j, encapsulated in the row vector $\mathbf{b}=[b_1,\ldots,b_{N_s}]$, are the amplitudes of the correction spectra. In summary, the differential radiance models can be outlined as follows.

1. In DRMI we solve the nonlinear equation

$$R^{\delta}_{\mathrm{mes}}(\lambda_k)=R_{\mathrm{sim}}(\lambda_k,\mathbf{X})+\sum_{j=1}^{N_s}b_jS_j(\lambda_k,\mathbf{X}_a),\ k=1,\ldots,N_\lambda, \tag{21}$$

for the state vector $\mathbf{x}=[\mathbf{X},\mathbf{b}]^T$, where $R^{\delta}_{\mathrm{mes}}(\lambda_k)$ and $R_{\mathrm{sim}}(\lambda_k,\mathbf{X})$ are the measured and simulated differential spectral signals defined, respectively, by

$$R^{\delta}_{\mathrm{mes}}(\lambda_k)=\ln \mathrm{I}^{\,\delta}_{\mathrm{mes}}(\lambda_k)-P_{\mathrm{mes}}(\lambda_k,\mathbf{c}_{\mathrm{mes}}), \tag{22}$$

$$R_{\mathrm{sim}}(\lambda_k,\mathbf{X})=\ln \mathrm{I}_{\,\mathrm{sim}}(\lambda_k,\mathbf{X})-P_{\mathrm{sim}}(\lambda_k,\mathbf{c}_{\mathrm{sim}}(\mathbf{X})). \tag{23}$$

Here, $P_{\mathrm{mes}}(\lambda,\mathbf{c}_{\mathrm{mes}})$ and $P_{\mathrm{sim}}(\lambda,\mathbf{c}_{\mathrm{sim}}(\mathbf{X}))$ are polynomials, which account for the low-order spectral structure due to cloud and aerosol scattering, and also (partially) compensate for uncertainties in the surface albedo. The coefficients $\mathbf{c}_{\mathrm{mes}}$ and $\mathbf{c}_{\mathrm{sim}}(\mathbf{X})$ of the smoothing polynomials $P_{\mathrm{mes}}(\lambda,\mathbf{c}_{\mathrm{mes}})$ and $P_{\mathrm{sim}}(\lambda,\mathbf{c}_{\mathrm{sim}}(\mathbf{X}))$, respectively, are computed as the solutions of the least-squares problems

$$\mathbf{c}_{\mathrm{mes}}=\arg\min_{\mathbf{c}}\sum_{k=1}^{N_\lambda}[\ln \mathrm{I}^{\,\delta}_{\mathrm{mes}}(\lambda_k)-P_{\mathrm{mes}}(\lambda_k,\mathbf{c})]^2 \tag{24}$$

and

$$\mathbf{c}_{\mathrm{sim}}(\mathbf{X})=\arg\min_{\mathbf{c}}\sum_{k=1}^{N_\lambda}[\ln \mathrm{I}_{\,\mathrm{sim}}(\lambda_k,\mathbf{X})-P_{\mathrm{sim}}(\lambda_k,\mathbf{c})]^2, \tag{25}$$

respectively. Thus, these coefficients, which are uniquely determined by $\ln \mathrm{I}^{\,\delta}_{\mathrm{mes}}(\lambda_k)$ and $\ln \mathrm{I}_{\,\mathrm{sim}}(\lambda_k,\mathbf{X})$, are not a part of the retrieval.

2. In DRME we solve the nonlinear equation

$$R^{\delta}_{\mathrm{mes}}(\lambda_k)=\ln \mathrm{I}_{\,\mathrm{sim}}(\lambda_k,\mathbf{X})+\sum_{j=1}^{N_s}b_jS_j(\lambda_k,\mathbf{X}_a)-P(\lambda_k,\mathbf{c}),\ k=1,\ldots,N_\lambda, \tag{26}$$

for the state vector $\mathbf{x}=[\mathbf{X},\mathbf{b},\mathbf{c}]^T$, where $P(\lambda,\mathbf{c})$ is a smoothing polynomial. Here, the coefficients $\mathbf{c}$ of the smoothing polynomial $P(\lambda,\mathbf{c})$ are included in the retrieval.

The efficiency of DRME can be increased by considering the linearization

$$\ln \mathrm{I}_{\,\mathrm{sim}}(\lambda_k,\mathbf{X})=\ln \mathrm{I}_{\,\mathrm{sim}}(\lambda_k,\mathbf{X}_a)+\sum_{g=1}^{N_g}(X_g-X_{ag})\frac{\partial \ln \mathrm{I}_{\,\mathrm{sim}}}{\partial X_g}(\lambda_k,\mathbf{X}_a)+\varepsilon_{\mathrm{lin}}(\lambda_k,\mathbf{X}-\mathbf{X}_a), \tag{27}$$

where $\varepsilon_{\mathrm{lin}}(\lambda_k,\mathbf{X}-\mathbf{X}_a)$ is the linearization error, so that, under the assumption that $\varepsilon_{\mathrm{lin}}$ is negligible, we are led to the solution of the linear equation

$$R^{\delta}_{\mathrm{mes}}(\lambda_k)=\ln \mathrm{I}_{\,\mathrm{sim}}(\lambda_k,\mathbf{X}_a)+\sum_{g=1}^{N_g}(X_g-X_{ag})\frac{\partial \ln \mathrm{I}_{\,\mathrm{sim}}}{\partial X_g}(\lambda_k,\mathbf{X}_a)+\sum_{j=1}^{N_s}b_jS_j(\lambda_k,\mathbf{X}_a)-P(\lambda_k,\mathbf{c}),\ k=1,\ldots,N_\lambda. \tag{28}$$

1.2.2 Differential Optical Absorption Spectroscopy

Eq. (28) is equivalent with the DOAS equation [11],

$$\ln \mathrm{I}^{\,\delta}_{\mathrm{mes}}(\lambda_k)=-\sum_{g=1}^{N_g}S_g\,\overline{C}_{\mathrm{absg}}(\lambda_k)+\sum_{j=1}^{N_s}b_jS_j(\lambda_k)+P(\lambda_k,\mathbf{c}),\ k=1,\ldots,N_\lambda, \tag{29}$$

which is solved for the state vector $\mathbf{x}=[\mathbf{S},\mathbf{b},\mathbf{c}]^T$, where $\mathbf{S}=[S_1,\ldots,S_{N_g}]^T$, S_g is the slant column of gas g, and

$$\overline{C}_{\mathrm{absg}}(\lambda_k)=\frac{1}{\int_0^{L_z} n_g(z)\mathrm{d}z}\int_0^{L_z} C_{\mathrm{absg}}(\lambda_k,z)n_g(z)\mathrm{d}z \tag{30}$$

the altitude-averaged absorption cross section of gas g at wavelength λ_k. The total column X_g is then computed from the slant column S_g by means of the relation

$$S_g=A(X_{\mathrm{ag}})X_g, \tag{31}$$

where $A(X_{\mathrm{ag}})$ is the air-mass factor of gas g. Note that in the classical DOAS, the slant column and the air-mass factor are assumed to be wavelength independent, and that the air-mass factor is defined with respect to the a priori. At a reference wavelength λ_0, the air-mass factor is computed as (cf. Eqs. (20), (27), (29), and (31))

$$\mathrm{A}(X_{\mathrm{ag}})=-\frac{1}{\overline{C}_{\mathrm{absg}}(\lambda_0)}\frac{\partial \ln \mathrm{I}_{\mathrm{sim}}}{\partial X_g}(\lambda_0,\mathbf{X}_{\mathrm{a}}). \tag{32}$$

To calculate $\partial \ln I_{\mathrm{sim}}/\partial X_g$, the scale profile approximation is used, i.e., if s_g is the scale factor of gas g, we have $x_{g,j}=s_g x_{\mathrm{ag},j}$, for all $j=1,\ldots,N_{\mathrm{lay}}$. Consequently, we find $s_g=x_{g,j}/x_{\mathrm{ag},j}=X_g/X_{\mathrm{ag}}$, yielding the one-to-one correspondence $x_{g,j}=(X_g/X_{\mathrm{ag}})x_{\mathrm{ag},j}$, and further,

$$\frac{\partial \mathrm{I}_{\mathrm{sim}}}{\partial X_g}(\lambda,\mathbf{X}_{\mathrm{a}})=\sum_{j=1}^{N_{\mathrm{lay}}}\left(\frac{\partial \mathrm{I}_{\mathrm{sim}}}{\partial x_{g,j}}\frac{\partial x_{g,j}}{\partial X_g}\right)(\lambda,\mathbf{X}_{\mathrm{a}})=\frac{1}{X_{\mathrm{ag}}}\sum_{j=1}^{N_{\mathrm{lay}}}\frac{\partial \mathrm{I}_{\mathrm{sim}}}{\partial x_{g,j}}(\lambda,\mathbf{X}_{\mathrm{a}})x_{\mathrm{ag},j}. \tag{33}$$

An alternative representation for the air-mass factor is

$$\mathrm{A}(X_{\mathrm{ag}})=\frac{1}{X_{\mathrm{ag}}}\sum_{j=1}^{N_{\mathrm{lay}}}\mathrm{A}_j(X_{\mathrm{ag}})x_{\mathrm{ag},j}, \tag{34}$$

where

$$\mathrm{A}_j(X_{\mathrm{ag}})=-\frac{1}{\overline{C}_{\mathrm{absg}}(\lambda_0)}\frac{\partial \ln \mathrm{I}_{\mathrm{sim}}}{\partial x_{g,j}}(\lambda_0,\mathbf{X}_{\mathrm{a}}) \tag{35}$$

is the box air-mass factor on the layer j.

Some comments can be made here.

1. The expression of the air-mass factor given by Eq. (32) with $\partial \ln \mathrm{I}_{\mathrm{sim}}/\partial X_g$ as in Eq. (33) is identical to that given by Eq. (34) with $\mathrm{A}_j(X_{\mathrm{ag}})$ as in Eq. (35). Thus, representation (34) in conjunction with (35) tacitly assumes the scale profile approximation.
2. The DOAS model is a parcicular case of the linearized version of DRME (28) when the partial derivative $\partial \ln \mathrm{I}_{\mathrm{sim}}/\partial X_g$ is computed at a reference wavelength. In fact, the DOAS model is less accurate than the differential radiance models (it incorporates the maximum number of simplifications that can be made), but it is much more efficient.

1.3 Retrieval algorithms

Retrieval algorithms have been designed by combining a radiative transfer model with an inverse model. In other words, a three-dimensional or an approximate radiative transfer model is combined with a differential radiance or a DOAS model as shown in Table 1. The resulting algorithms have some peculiarities, which are summarized below.

Table 1. **Retrieval algorithms combining different radiative transfer models and inverse models**

	Radiative transfer model	Inverse Model
3D	SHDOM	
1D	Tilted independent column approximation (TICA)	Differential radiance model with internal smoothing (DRMI)
2D	Independent slice approximation (ISA)	Differential radiance model with external smoothing (DRME)
	Nonlocal independent slice approximation (NISA)	Differential optical absorption spectroscopy (DOAS)
	Zeroth-order stochastic model (STH)	

1. A physical-based retrieval algorithm requires the knowledge of the partial derivatives of the radiance with respect to the atmospheric parameters to be retrieved. These are provided by a linearization model. Linearizations of SHDOM by means of a forward and a forward-adjoint approach have been discussed in Ref. [12], and can be summarized as follows.

(a) The linearized forward-adjoint approach relies on the application of the adjoint radiative transfer theory. The method requires less storage for derivatives calculation, are much faster, but relatively less accurate. The main reason for this lower accuracy is that different interpolation schemes are used for radiance and derivative calculations.

(b) The linearized forward approach relies on an analytical computation of the derivatives. The method is accurate and has the advantage that no assumptions rather than those of the forward model have to be made. However, the method is time consuming and memory demanding when the number of parameters to be retrieved is large. The reason is that not only the source function has to be stored as a spherical harmonic series at each grid point, but also its derivatives with respect to the atmospheric parameters of interest. However, because in the present application, the number of retrieved quantities is relatively small, we decided in the favor of the linearized forward approach. Specifically, the partial derivatives are computed in an analytical manner by using the chain rule in a sort of backward procedure starting with the output radiance and following the chain of dependencies back to the inputs to the model. Note that in SHDOM, the absorption coefficient is specified on levels, i.e., $\sigma_{\mathrm{absg}}^{\mathrm{gas}}(\lambda, z_j) = C_{\mathrm{absg}}(\lambda, z_j) n_g(z_j)$, and under the scale profile approximation, we find $\sigma_{\mathrm{absg},j}^{\mathrm{gas}}(\lambda) = (X_g / X_{\mathrm{ag}}) \sigma_{\mathrm{absag},j}^{\mathrm{gas}}(\lambda)$ and consequently,

$$\frac{\partial \mathrm{I}_{\mathrm{sim}}}{\partial X_g}(\lambda, \mathbf{X}_{\mathrm{a}}) = \frac{1}{X_{\mathrm{ag}}} \sum_{j=1}^{N_z} \frac{\partial \mathrm{I}_{\mathrm{sim}}}{\partial \sigma_{\mathrm{absg},j}^{\mathrm{gas}}}(\lambda, \mathbf{X}_{\mathrm{a}}) \sigma_{\mathrm{absag},j}^{\mathrm{gas}}(\lambda), \tag{36}$$

where $\sigma_{\mathrm{absg},j}^{\mathrm{gas}}(\lambda) = \sigma_{\mathrm{absg}}^{\mathrm{gas}}(\lambda, z_j)$. Thus, the computation of the partial derivative with respect to the total column requires a linearization of SHDOM with respect to the absorption coefficient.

2. To speed up the computations, the linearized SHDOM is equipped with a spectral acceleration approach that combines the correlated k-distribution method with dimensionality reduction techniques. This approach was applied for computing the spectral signal in Ref. [13], and extended to derivative calculations in Ref. [10].

3. The iteratively regularized Gauss–Newton method is used as inversion (regularization) approach to solve the (ill-posed) nonlinear equations (21) and (26) [14]. In this approach, (i) the regularization matrix is chosen as a diagonal matrix, (ii) the penalty term is gradually decreased during the iterative process by choosing the regularization parameters as the terms of a decreasing sequence, and (iii) the iterative process is stopped according to the discrepancy principle, that is, when the residual is below the noise level. As compared to the method of Tikhonov regularization, the iteratively regularized Gauss–Newton method does not require the knowledge of an optimal value of the regularization parameter, is less affected by overestimations of the regularization parameter, but needs more iterations to converge.

4. The retrieval algorithms are based on the assumption that the cloud extinction field, as well as, the phase function are available at a high spatial resolution. However, in order to simplify the numerical

analysis, the clouds are considered to be homogeneous in the vertical direction. In this case, the retrieval algorithms will deal with broken cloud fields that fulfill this condition.

1.4 Generation of test scenarios for multi-dimensional broken cloud fields

In this section we assess the accuracy and efficiency of the algorithms for retrieving total column amount of NO_2 under cloudy conditions. More precisely, we analyze the retrieval algorithms relying on

1. a three-dimensional radiative transfer model, namely, SHDOM (Section 1.1.1),
2. an approximate one-dimensional radiative trasnfer models, namely, the titled independent column approximation (Section 1.1.2), and
3. approximate two-dimensional radiative transfer models (Section 1.1.3), namely,
   (a) the independent slice approximation,
   (b) the nonlocal independent slice approximation, and
   (c) a zeroth-order stochastic model for two-dimensional geometries.

1.4.1 Retrieval algorithm based on a three-dimensional radiative transfer model

We begin our numerical analysis by considering a retrieval algorithm based on a three-dimensional radiative transfer model SHDOM. In the simulations, the geometrical and optical parameters are chosen as follows.

1. The domain of analysis is a rectangular prism of lengths $L_x = L_y = 15$ km and $L_z = 50$ km. The discretization steps along the horizontal directions are $\Delta x = \Delta y = 0.5$ km. Along the vertical direction, the atmosphere between 0 and 50 km is discretized with a step of 0.5 km between 0 and 3 km, 0.1 km between 3 and 4 km, 0.5 km between 4 and 10 km, 1.0 km between 10 and 14 km, 2 km between 14 and 30 km, and 5 km between 30 and 50 km.

2. A homogeneous cloud is placed between 3 and 4 km. The cloud extinction field is given by $\sigma_{\text{ext}}^{\text{cloud}}(x,y) = \sigma_0 f(x,y)$, where $\sigma_0 = 6\ \text{km}^{-1}$ and $f(x,y)$ is the indicator function (note that $f(x,y)$ takes the values 1 and 0 inside and outside the cloud, respectively). The cloud phase function is a Henyey–Greenstein phase function with the asymmetry parameter $g = 0.8$, and the cloud single-scattering albedo is $\omega_{\text{cloud}} = 0.99$. Eight cloudy scenes are generated by a two-dimensional broken cloud model [15] with a cloud fraction of about 0.4. The extinction field $\sigma_{\text{ext}}^{\text{cloud}}(x,y)$ is smoothed at the boundary of a cloudy region in order to avoid abrupt changes in the horizontal plane. The indicator functions corresponding to the eight cloudy scenes are illustrated in Figure 2.

3. The footprint of the detector is a square of length $2a = 10\Delta x$ centered at $x_0 = y_0 = L_x/2$, and $z_0 = L_z$, and a wavelength-dependent slit function corresponding to the TROPOMI instrument is assumed. The solar and instrument zenith angles are $\theta_0 = 30^\circ$ and $\theta_{\text{m}}^0 = 45^\circ$, respectively, and the relative azimuth angle is $\Delta\varphi = 0$. A Lambertian reflecting surface with the surface albedo $A = 0.2$ is considered.

4. In addition to the scattering and absorption by the cloud, molecular Rayleigh scattering and the absorption by NO_2, ozone (O_3), oxygen dimer (O_4), and water vapor (H_2O) are considered. Rayleigh scattering cross-sections are calculated using the parametrization by Bodhaine et al. [20], while the absoprtion cross-sections for NO_2, O_3 and O_4 are taken from Refs. [21], [22], and [23], respectively. The measurement spectral grid roughly resembles the TROPOMI's spectral resolution and consists of 119 spectral points between 425 nm and 450 nm.

5. In SHDOM, the numbers of discrete zenith and azimuth angles are $N_\mu = 16$ and $N_\varphi = 2N_\mu$, respectively, the spherical harmonics truncation indices are $N = N_\mu - 1$ and $M = N_\varphi / 2 - 1$, and the delta-M scaling method, the TMS correction, and an adaptive grid with a splitting accuracy of 10^{-4} are used.

The process of generating synthetic measurement spectra is organized as follows.

1. To generate the true (exact) partial column profile we use an a priori partial column profile of NO_2 corresponding to a polluted scenario [16]. In this regard, denoting the a priori partial columns of gas g by $x_{\mathrm{ag},j}$, we choose the true partial columns as $x^\dagger_{g,j} = s_g x_{\mathrm{ag},j}$, $j = 1,\ldots,N_\mathrm{z}$ with $s_{\mathrm{NO}_2} = 2.0$ and $s_{\mathrm{O}_3} = s_{\mathrm{O}_4} = s_{\mathrm{H}_2\mathrm{O}} = 1.2$. The reason for this choice is that we are primarily interested in the retrieval of the main gas NO_2 and less of the auxiliary gases. In fact, the auxiliary gases can be included in the retrieval or not. If they are not included, they can be treated as forward model parameter errors, and thus, can be used to quantify the total retrieval error. The true total column $X^\dagger_g$ of gas g is then computed as $X^\dagger_g = \sum_{j=1}^{N_z} x^\dagger_{g,j} = s_g X_{\mathrm{ag}}$; thus, $X^\dagger_{\mathrm{NO}_2} = 2X_{\mathrm{aNO}_2}$.

2. For $\mathbf{X}^\dagger = [X^\dagger_{\mathrm{NO}_2}, X^\dagger_{\mathrm{O}_3}, X^\dagger_{\mathrm{O}_4}, X^\dagger_{\mathrm{H}_2\mathrm{O}}]$, we generate the simulated spectral signal $\mathrm{I}_{\mathrm{sim}}(\lambda_k, \mathbf{X}^\dagger)$ by means of SHDOM.

3. For cubic smoothing polynomials, we determine the coefficients $\mathbf{c}_{\mathrm{sim}}(\mathbf{X}^\dagger)$ of the polynomial $P_{\mathrm{sim}}(\lambda, \mathbf{c}_{\mathrm{sim}}(\mathbf{X}^\dagger))$ as the solutions of the least-squares problem (25) [17].

4. We compute the noisy spectral signal as $\mathrm{I}^{\,\delta}_{\mathrm{sim}}(\lambda_k, \mathbf{X}^\dagger) = \mathrm{I}_{\mathrm{sim}}(\lambda_k, \mathbf{X}^\dagger) + \delta_k$, where the measurement errors δ_k are assumed to be independent Gaussian random variables with zero mean and standard deviation $\sigma_k = \mathrm{I}_{\mathrm{sim}}(\lambda_k, \mathbf{X}^\dagger)/\mathrm{SNR}$, where SNR is the signal-to-noise ratio. It should be pointed out that in view of the approximation

$$\ln \mathrm{I}^{\,\delta}_{\mathrm{sim}}(\lambda_k, \mathbf{X}^\dagger) \approx \ln \mathrm{I}_{\mathrm{sim}}(\lambda_k, \mathbf{X}^\dagger) + \frac{\delta_k}{\mathrm{I}_{\mathrm{sim}}(\lambda_k, \mathbf{X}^\dagger)}, \tag{37}$$

the error in $\ln \mathrm{I}^{\,\delta}_{\mathrm{sim}}(\lambda_k, \mathbf{X}^\dagger)$ is $\delta_{\ln k} = \delta_k / \mathrm{I}_{\mathrm{sim}}(\lambda_k, \mathbf{X}^\dagger)$ yielding $\sigma_{\ln k} = 1/\mathrm{SNR}$ for all k. In other words, the measurement error vector is white noise with the covariance matrix $(1/\mathrm{SNR}^2)\mathbf{I}_m$, where $\mathbf{I}_m$ is the identity matrix. Because in our simulations we are mainly interested in multi-dimensional effects, we take $\mathrm{SNR} = 10^4$, that is, we assume an almost perfect instrument and neglect the forward model errors.

5. We include the Ring correction spectrum $S_\mathrm{R}(\lambda_k, \mathbf{X}_\mathrm{a})$ illustrated in Figure 3 in the retrieval, and choose the a priori and true Ring amplitudes as $b_{\mathrm{aR}} = 5\times10^{-2}$ and $b^\dagger_\mathrm{R} = 2b_{\mathrm{aR}}$, respectively. Note that the inelastic scattering is described by a first-order Rayleigh scattering model, i.e., by applying a first-order iteration scheme to the one-dimensional radiative transfer equation for inelastic scattering [18].

6. For DRMI, we compute the measured differential spectral signal as

$$R^\delta_{\mathrm{mes}}(\lambda_k) = [\ln \mathrm{I}^{\,\delta}_{\mathrm{sim}}(\lambda_k, \mathbf{X}^\dagger) - P_{\mathrm{sim}}(\lambda, \mathbf{c}_{\mathrm{sim}}(\mathbf{X}^\dagger))] + b^\dagger_\mathrm{R} S_\mathrm{R}(\lambda_k, \mathbf{X}_\mathrm{a}), \tag{38}$$

while for DRME, we choose $\mathbf{c}^\dagger = 0.5\mathbf{c}_{\mathrm{sim}}(\mathbf{X}^\dagger)$ and compute the measured differential spectral signal as

$$R^\delta_{\mathrm{mes}}(\lambda_k) = \ln \mathrm{I}^{\,\delta}_{\mathrm{sim}}(\lambda_k, \mathbf{X}^\dagger) + b^\dagger_\mathrm{R} S_\mathrm{R}(\lambda_k, \mathbf{X}_\mathrm{a}) - P(\lambda_k, \mathbf{c}^\dagger). \tag{39}$$

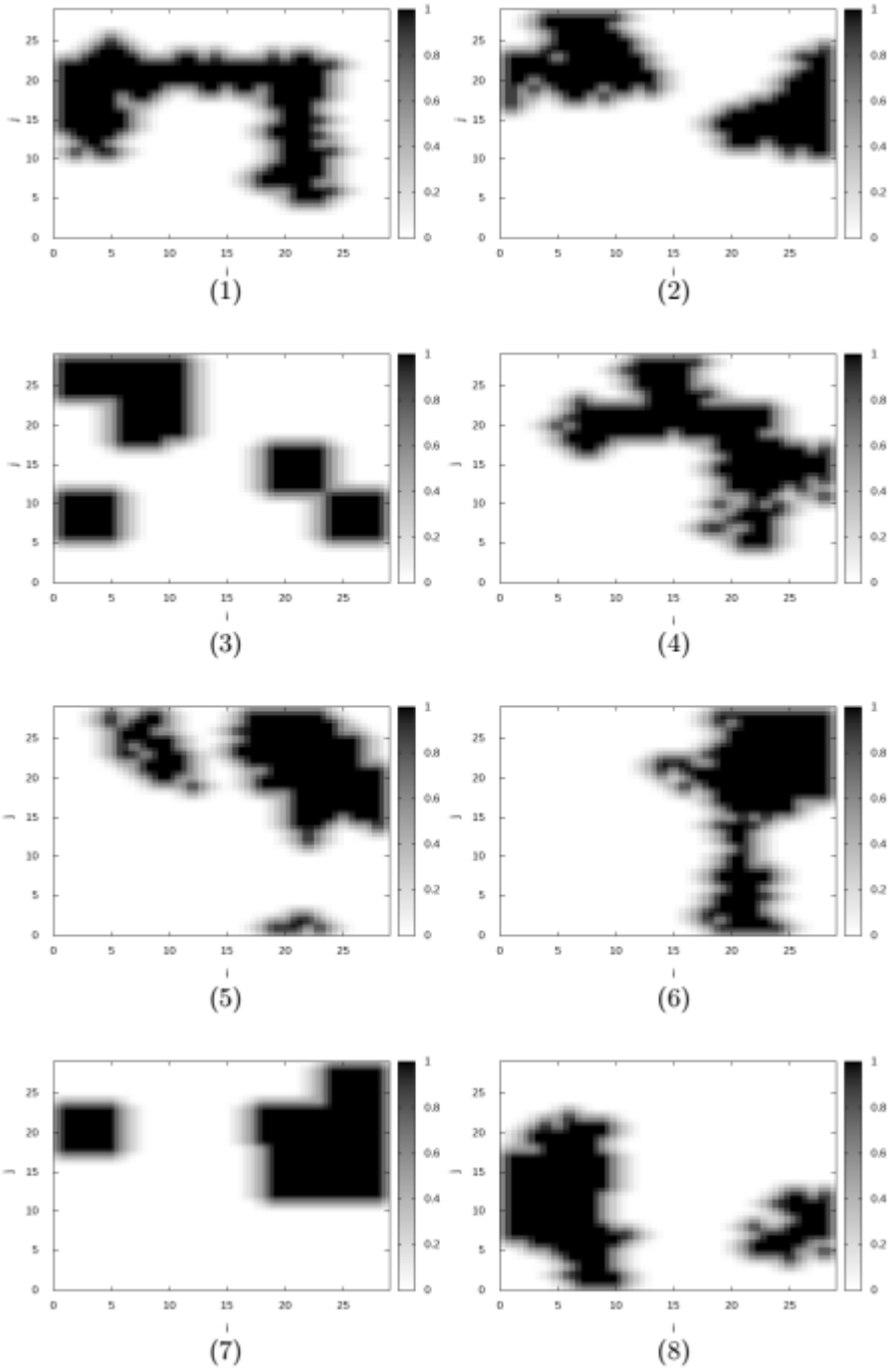

Figure 2. Indicator function $f(x_i, y_j)$ with $x_i = i\Delta x$ and $y_j = j\Delta y$ for the 8 cloudy scenes.

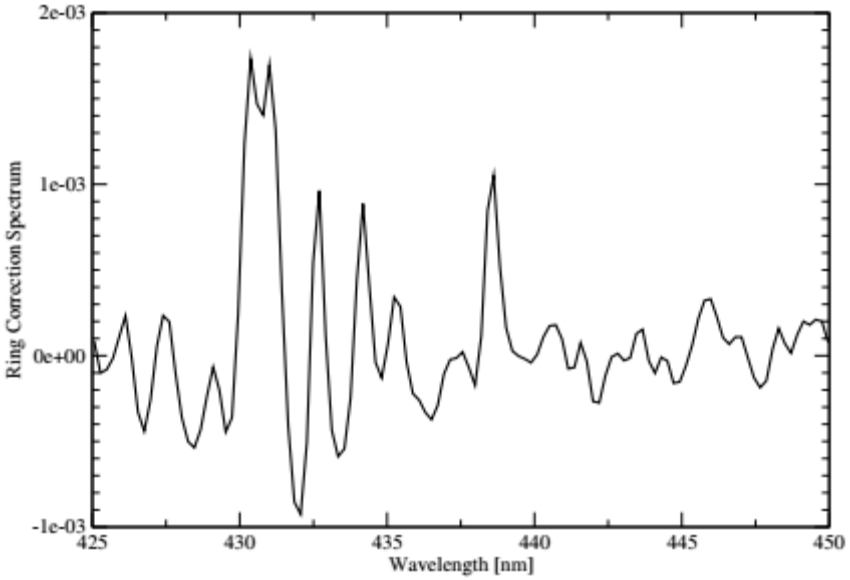

Figure 3. Ring correction spectrum included in the retrieval.

In Table 2 we illustrate the relative errors for the cloudy scenes considered in Figure 2. Note that both the measured and simulated spectral signals are computed by a three-dimensional radiative transfer model. As inverse models, the two differential radiance models DRMI and DRME are used. The relative errors are smaller than 0.05%, but the computation time is extremely high; on a computer Intel(R) Core(TM) i5-3340M CPU @ 2.70GHz with 7858Mb RAM, the computation time is of about 14 hours and 15 minutes. Nevertheless, the main conclusion of the numerical analysis is that although for three-dimensional geometries, the computational time is high, the main concepts of the algorithm are correct and the retrieval results are accurate.

Table 2. Relative errors and the computation times (CPU) in hours:minutes:seconds for the retrieval algorithm based on a three-dimensional radiative transfer model. The results correspond to the Differential Radiance Model with Internal smoothing (DRMI) and the Differential Radiance Model with Extrnal smoothing (DRME).

Cloudy Scene	DRMI		DRME	
	Rel. Errors	CPU	Rel. Errors	CPU
1	4.74×10^{-4}	14:20:32	4.70×10^{-4}	14:15:31
2	3.00×10^{-4}	14:28:21	3.04×10^{-4}	14:21:43
3	1.52×10^{-4}	14:21:26	1.35×10^{-4}	14:15:57
4	5.53×10^{-4}	14:11:14	6.02×10^{-4}	14:05:18
5	3.13×10^{-4}	14:22:07	3.63×10^{-4}	14:15:23
6	1.67×10^{-4}	14:21:16	1.46×10^{-4}	14:14:36
7	2.43×10^{-4}	14:21:33	2.12×10^{-4}	14:09:41
8	1.92×10^{-4}	14:27:03	1.88×10^{-4}	14:20:13

1.4.2 Retrieval algorithms based on approximate radiative transfer models

In this section we analyze the accuracy and efficiency of the retrieval algorithm with approximate radiative transfer models. The main focus is on two-dimensional radiative transfer models, and in particular,

on cloud shadow effects under polluted conditions. The cloud scenarios and the parameters of simulation are chosen as follows.

1. The lengths of the domain of analysis in the shape of a rectangular prism are $L_x = L_y = 30$ km and $L_z = 50$ km, and the discretization steps along the x- and y-axis are $\Delta x = \Delta y = 1$ km (similar to the VIIRS spatial resolution). A cloud with the extinction field $\sigma_{ext}^{cloud}(x,y,z) = \sigma_0 f(x,y)$, where $f(x,y)$ is the indicator function taking the values 1 and 0 inside and outside the cloud, respectively, is placed between 4 and 5 km; thus, the cloud is homogeneous in the vertical direction and has the geometrical thickness $\Delta H = 1$ km. The fifteen cloud scenes considered in our numerical analysis and illustrated in Figure 4 have a variability along the y-axis and are chosen such that the solar direction is along the x-axis (in a preprocessing step, the cloud scene should eventually be rotated to fulfill this requirement).

2. The cloud single-scattering albedo and the phase function are computed by Mie theory at a wavelength of 437.56 nm and for a Gamma size distribution with a modal radius of 6.66 μm and a Gamma size distribution parameter of 6 (the effective radius is 10 μm). The calculations are performed for a mid-latitude summer atmosphere [19]. As in the previous simulations, molecular Rayleigh scattering and the absorption by NO_2, ozone (O_3), oxygen dimer (O_4), and water vapor (H_2O) are taken into account.

3. The footprint of the instrument, in the shape of a rectangle with lengths $l_x = 7$ km and $l_y = 4$ km, centered at $x_0 = y_0 = L_x/2$, and $z_0 = L_z$, is almost cloud-free but affected by the neighboring clouds shadows. The instrument zenith angle is $\theta_m = 0°$, the relative azimuth angle is $\Delta\varphi = 0$, and a Lambertian reflecting surface with the surface albedo $A = 0.05$ is chosen.

4. The measurement spectral grid ranging between 425 nm and 450 nm consists of 119 spectral points, and the wavelength dependent slit function of the instrument corresponds to the TROPOMI instrument.

5. In SHDOM, the numbers of discrete zenith and azimuth angles are $N_\mu = 32$ and $N_\varphi = 2N_\mu$, respectively, the spherical harmonics truncation indices are $N = N_\mu - 1$ and $M = N_\varphi/2 - 1$, and the delta-M scaling method, the TMS correction, and an adaptive grid with a splitting accuracy of 10^{-3} are used.

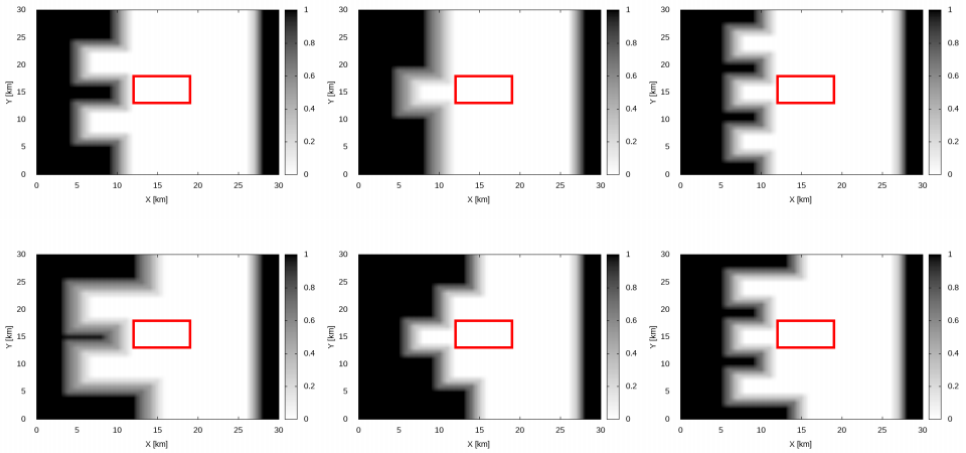

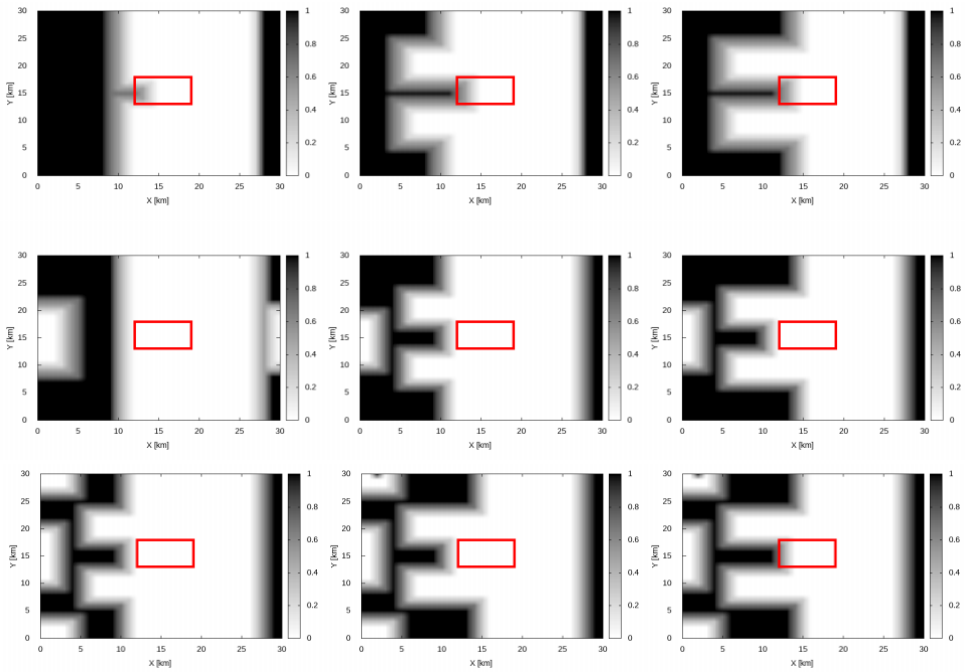

Figure 4. Indicator function $f(x,y)$ for the 15 cloudy scenes. At the boundary of a cloudy region, the extinction field is smoothed in order to avoid abrupt changes in the horizontal plane. The red rectangle visualizes the footprint of the instrument.

1.4.3 First Test example

In the first test example we generate synthetic measurement spectra for a three-dimensional cloud scene and retrieve the total column of $\mathrm{NO_2}$ by using approximate radiative transfer models. As inverse model, the differential radiance model with external smoothing (DRME) is used. To generate a synthetic measurement we proceed as in Section 2.1. Specifically,

1. for $\mathrm{NO_2}$, we choose as true partial column profile a scaled version of an apriori profile corresponding to a polluted scenario with the scaling factor $s_{\mathrm{NO_2}} = 2.0$, i.e., $x^{\dagger}_{\mathrm{NO_2},j} = s_{\mathrm{NO_2}} x_{\mathrm{aNO_2},j}$, $j = 1,\ldots,N_{\mathrm{lay}}$, and compute the true total column as $X^{\dagger}_{\mathrm{NO_2}} = \sum_{j=1}^{N_{\mathrm{lay}}} x^{\dagger}_{\mathrm{NO_2},j}$; for auxiliary gases, we proceed analogously but with the scaling factors $s_{\mathrm{O_3}} = s_{\mathrm{O_4}} = s_{\mathrm{H_2O}} = 1.2$;

2. for the vector of true total columns $\mathbf{X}^{\dagger} = [X^{\dagger}_{\mathrm{NO_2}}, X^{\dagger}_{\mathrm{O_3}}, X^{\dagger}_{\mathrm{O_4}}, X^{\dagger}_{\mathrm{H_2O}}]$, we compute the simulated spectral signal $\mathrm{I}_{\mathrm{sim}}(\lambda_k, \mathbf{X}^{\dagger})$ with SHDOM, and generate the noisy spectral signal as $\mathrm{I}^{\delta}_{\mathrm{sim}}(\lambda_k, \mathbf{X}^{\dagger}) = \mathrm{I}_{\mathrm{sim}}(\lambda_k, \mathbf{X}^{\dagger}) + \delta_k$ with δ_k : $\mathrm{N}(0, \sigma_k^2)$ and $\sigma_k = \mathrm{I}_{\mathrm{sim}}(\lambda_k, \mathbf{X}^{\dagger}) / \mathrm{SNR}$, where $\mathrm{N}(\bar{x}, \sigma^2)$ stands for a normal distribution with mean $\bar{x}$ and variance σ^2, and $\mathrm{SNR} = 100$ is the signal-to-noise ratio;

3. for a cubic smoothing polynomials, we determine the coefficients $\mathbf{c}_{\mathrm{sim}}(\mathbf{X}^{\dagger})$ of the polynomial $P_{\mathrm{sim}}(\lambda, \mathbf{c}_{\mathrm{sim}}(\mathbf{X}^{\dagger}))$ as the solution of the least-squares problem $\mathbf{c}_{\mathrm{sim}}(\mathbf{X}^{\dagger}) = \arg\min_{\mathbf{c}} \sum_{k=1}^{N_\lambda} [\ln \mathrm{I}_{\mathrm{sim}}(\lambda_k, \mathbf{X}^{\dagger}) - P_{\mathrm{sim}}(\lambda_k, \mathbf{c})]^2$, and in the framework of the differential radiance model with internal smoothing, compute the measured differential spectral signal as

$$R^{\delta}_{\mathrm{mes}}(\lambda_k) = [\ln \mathrm{I}^{\delta}_{\mathrm{sim}}(\lambda_k, \mathbf{X}^{\dagger}) - P_{\mathrm{sim}}(\lambda, \mathbf{c}_{\mathrm{sim}}(\mathbf{X}^{\dagger}))] + b^{\dagger}_{\mathrm{R}} S_{\mathrm{R}}(\lambda_k, \mathbf{X}_{\mathrm{a}}), \tag{40}$$

where $S_R(\lambda_k, \mathbf{X}_a)$ is the Ring correction spectrum illustrated in Figure 3 and the a priori and true Ring amplitudes are chosen as $b_{aR} = 5\times10^{-2}$ and $b_R^{\dagger} = 2b_{aR}$, respectively.

In a first step, we compare

1. the independent slice approximation, and
2. the tilted independent column approximation.

Note that in the tilted independent column approximation, the direct radiation is calculated in the independent column (x_0, y_0) slanted toward the sun. In Figures 5-9, we illustrate the relative errors in the total column of NO_2 for 4 values of the cloud optical thickness $\tau = \sigma_0 \Delta H = 5,10,15,20$, and 2 values of the solar zenith angle $\theta_0 = 30^\circ, 60^\circ$. The plots show that

1. the relative errors of the tilted independent column approximation increase with increasing the cloud optical thickness and solar zenith angle, and can reach 20% (for the cloud scene 7, 8, and 9 when the instrument footprint is partially cloudy), while

2. the relative errors of the independent slice approximation increase in most cases with increasing the solar zenith angle and are almost below 5%.

On a computer Intel(R) Core(TM) i5-3340M CPU @ 2.70GHz with 7858Mb RAM, the computation times of the tilted independent column approximation and the independent slice approximation, corresponding to 3-4 iterations of the Gauss–Newton method, are 20-30 seconds and 6-8 minutes, respectively.

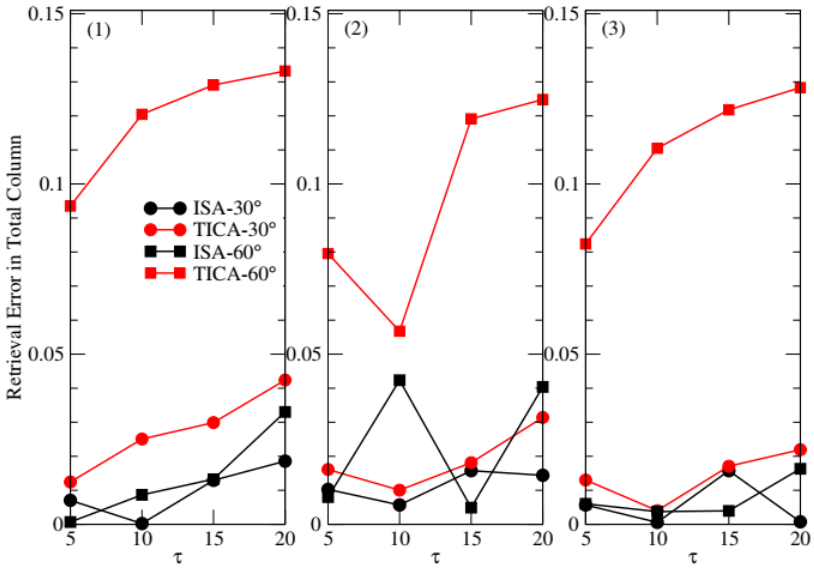

Figure 5. Relative error in total column of NO_2 for cloud optical thickness $\tau = 5,10,15,20$ and solar zenith angle $\theta_0 = 30^\circ, 60^\circ$. The results are computed for the cloud scenes 1, 2, and 3 by using the two-dimensional independent slice approximation (ISA) and the one-dimensional tilted independent column approximation

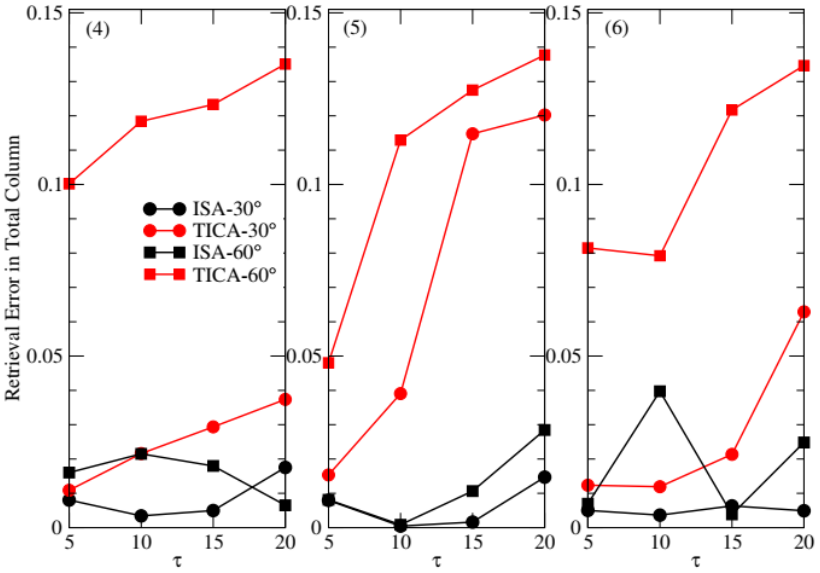

Figure 6. The same as in Figure 5 but for the cloud scenes 4, 5, and 6.

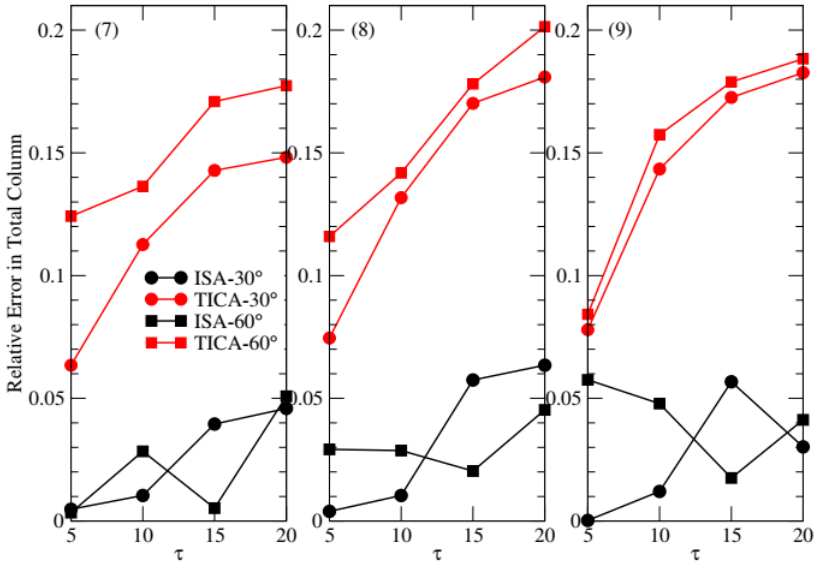

Figure 7. The same as in Figure 5 but for the cloud scenes 7, 8, and 9.

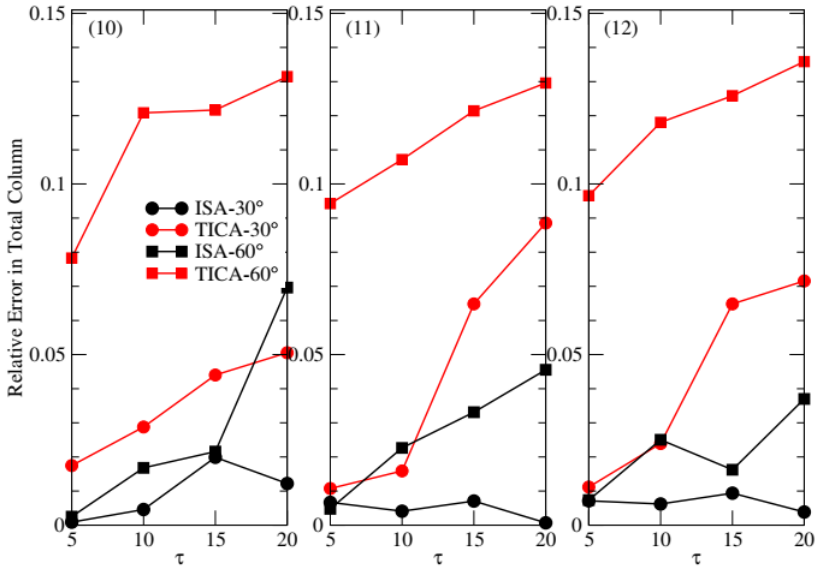

Figure 8. The same as in Figure 5 but for the cloud scenes 10, 11, and 12.

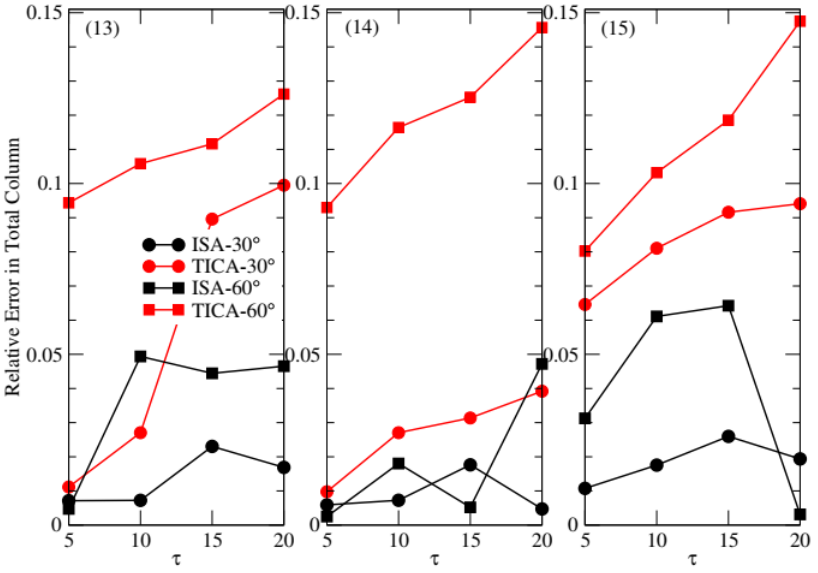

Figure 9. The same as in Figure 5 but for the cloud scenes 13, 14, and 15.

In a second step, we compare the two-dimensional radiative transfer models, namely,

1. the independent slice approximation,
2. the nonlocal independent slice approximation, and
3. the zeroth-order stochastic model.

In the nonlocal independent slice approximation, we choose $\ell = 10$ km, and compute $\mathrm{I}_{2\mathrm{D}}(\boldsymbol{\Omega}_{\mathrm{m}} \mid y)$ in Eq. (8) for 5 equidistant values of y in the interval $[y_0 - \ell, y_0 + \ell]$. The results illustrated in Figure 10 show that roughly speaking,

1. the zeroth-order stochastic model is the most accurate, and
2. the independent slice approximation has the lowest accuracy.

The computation times are 6-8 minutes for the independent pixel approximation, 35-40 minutes for the nonlocal independent slice approximation, and 25-30 minutes for the zeroth-order stochastic model. The

high computation time of the stochastic model is due to the fact that at each iteration step, the y-average transmission function $\langle T(\mathbf{r}_0,\mathbf{r})\rangle_y$ has to be computed. However, the small accuracy improvement obtained by the nonlocal independent slice approximation and the zeroth-order stochastic model (2% in the best case), does not justify the high computation times of these models.

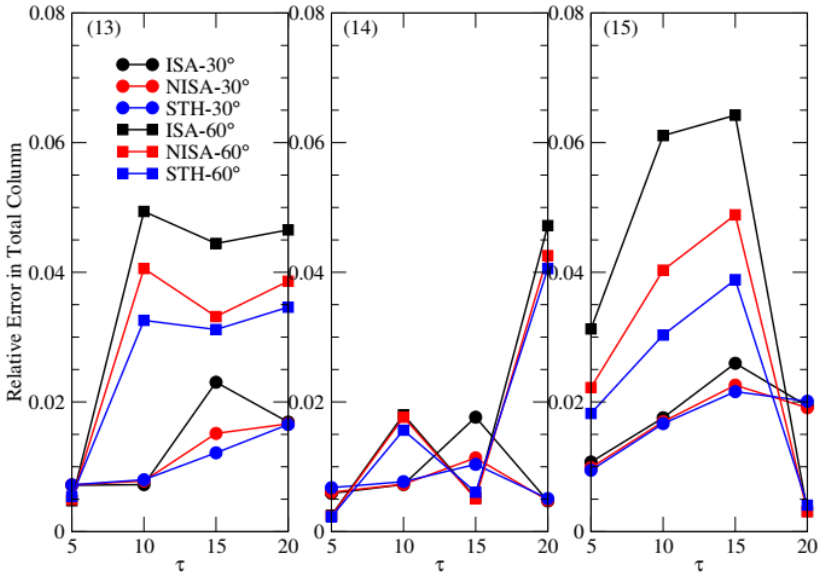

Figure 10. Relative error in total column of NO_2 for cloud optical thickness $\tau = 5,10,15,20$ and solar zenith angle $\theta_0 = 30^\circ, 60^\circ$. The results are computed for the cloud scenes 13, 14, and 15 by using the two-dimensional independent slice approximation (ISA), the nonlocal independent slice approximation (NISA) and the zeroth-order stochastic model (STH).

1.4.4 Second Test example

In the second test example we focus on the DOAS algorithm [section 1.2.2] and compare the air-mass factors of NO_2, computed by three- and two-dimensional radiative transfer models. Specifically, we estimate the errors in the air-mass factors computed with

1. the one-dimensional tilted independent column approximation, and
2. the two-dimensional independent slice approximation

using as a reference, the air-mass factors computed with the three-dimensional radiative transfer model SHDOM. Note that the DOAS algorithm is based on a linearization of $\ln \mathrm{I}_{\mathrm{sim}}(\lambda_k,\mathbf{X})$ around the a priori (cf. Eq. (27)), and that in principle, the method is equivalent with one iteration of the differential radiance model with external smoothing. Also note that in view of Eq. (31), the relative error in the total column is equal to the relative error in the air-mass factor, that is,

$$\varepsilon_X = \frac{X_{2D} - X_{3D}}{X_{3D}} = \frac{\mathrm{A}_{3D}(X_a) - \mathrm{A}_{2D}(X_a)}{\mathrm{A}_{2D}(X_a)}, \tag{41}$$

where A_{3D} and A_{2D} are the air-mass factors computed by a three- and a two-dimensional radiative transfer model. In Figures 11-15, we illustrate the relative errors in the air-mass factor of NO_2 for 4 values of the cloud optical thickness $\tau = 5,10,15,20$ and 2 values of the solar zenith angle $\theta_0 = 30^\circ, 60^\circ$. The results are computed with the independent slice approximation and the tilted independent column approximation at the wavelength $\lambda_0 = 437.56$ nm. The same conclusions as in the first test example can be drawn:

1. the relative errors of the tilted independent column approximation increase with increasing the solar zenith angle, and can even be 30% (for the cloud scene 7, 8, and 9), while
2. the relative errors of the independent slice approximation are in general below 4%.

The computation times are 10-20 seconds for the tilted independent column approximation and 1-3 minutes for the independent slice approximation.

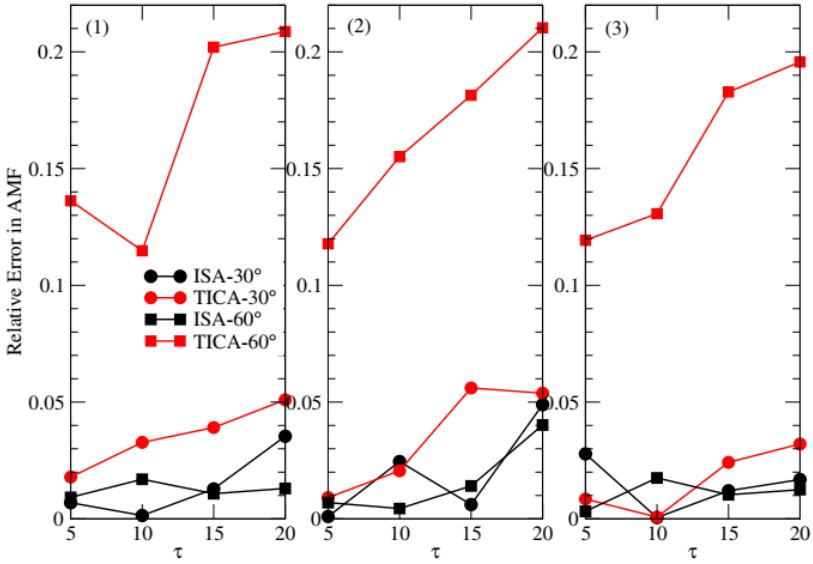

Figure 11. Relative error in air-mass factor for cloud optical thickness $\tau = 5,10,15,20$ and solar zenith angle $\theta_0 = 30^\circ, 60^\circ$. The results are computed for the cloud scenes 1, 2, and 3 by using the two-dimensional independent slice approximation (ISA) and the one-dimensional tilted independent column approximation (TICA).

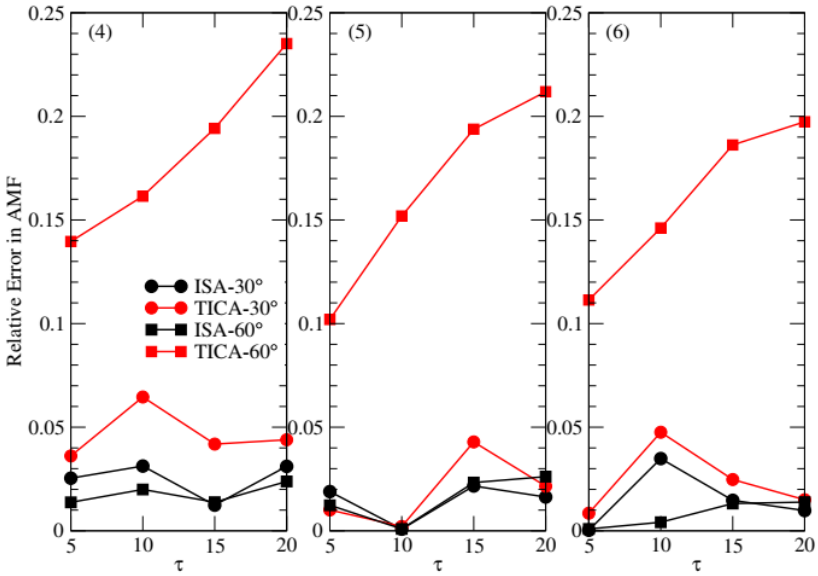

Figure 12. The same as in Figure 11 but for the cloud scenes 4, 5, and 6.

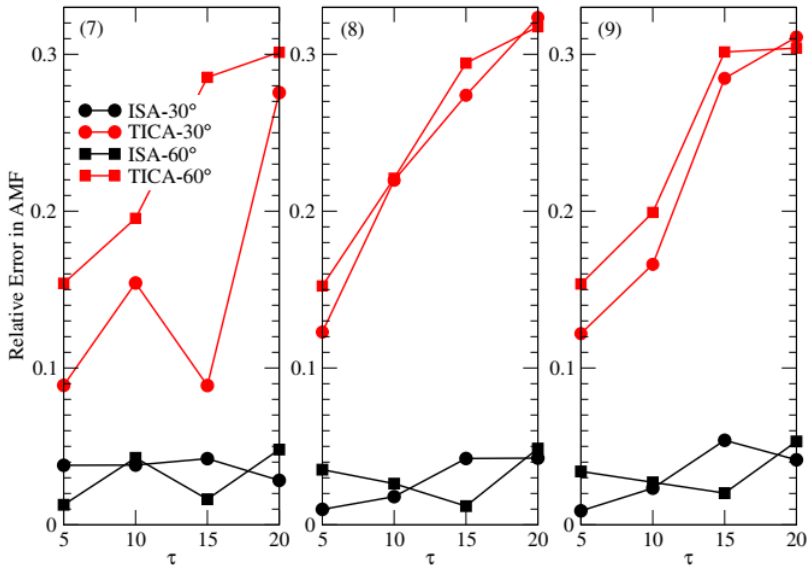

Figure 13. The same as in Figure 11 but for the cloud scenes 7, 8, and 9.

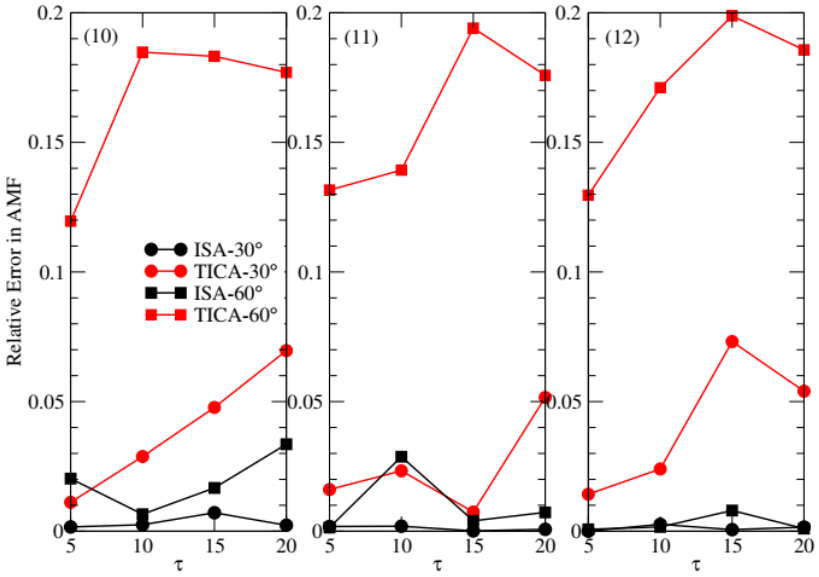

Figure 14. The same as in Figure 11 but for the cloud scenes 10, 11, and 12.

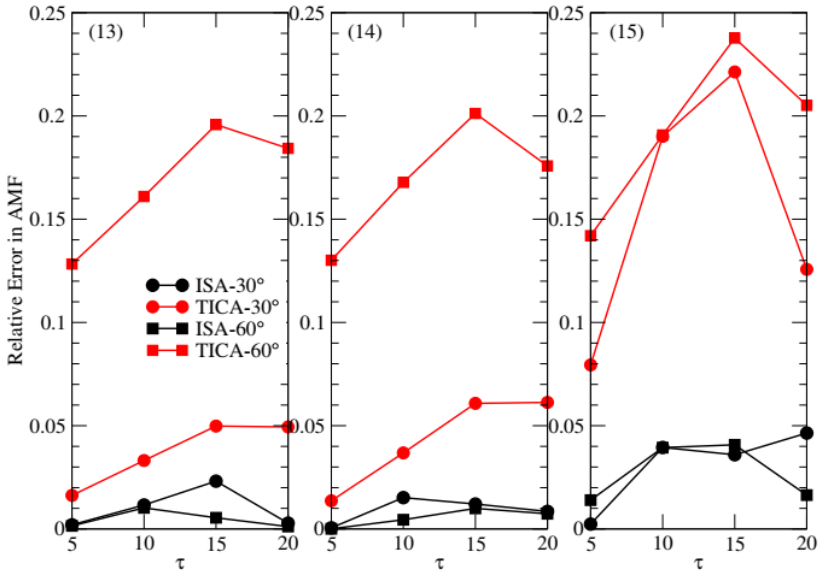

Figure 15. The same as in Figure 11 but for the cloud scenes 13, 14, and 15.

1.5 Discussion on the theoretical treatise

The accuracy and efficiency of several retrieval algorithms based on different radiative transfer models have been analyzed. The retrieval algorithms use (i) differential radiance models with internal and external smoothing, and the differential optical absorption spectroscopy algorithm as inverse models, (ii) the iteratively regularized Gauss-Newton method as regularization tool, and (iii) the linearized spherical harmonics discrete ordinate method as multi-dimensional radiative transfer model.

The numerical analysis related to the retrieval of the total column amount of NO_2 under cloudy conditions led to the following conclusions.

1. The three-dimensional radiative transfer model yields the highest accuracy (relative errors smaller than 0.05%). However, the extremely high computation time of about 14 hours disqualifies this method for processing a large amount of data.

2. The independent slice approximation with a computation time of 6-8 minutes and relative errors below 5% is a well balanced compromise between accuracy and efficiency.

3. The nonlocal independent slice approximation and a zeroth-order stochastic model yield relative errors of about 3-4%. However, the small accuracy improvement as compared to the independent splice approximation does not justify the high computation times of 25-40 minutes

4. The tilted independent column approximation with a computational time of 20-30 seconds can lead to large relative errors (of about 20%). Therefore, from the point of view of accuracy, the method is not recommended.

The numerical analysis related to the computation of the air-mass factor has shown that:

1. the relative errors of the independent slice approximation are below 4%, while the computation time is around 1-3 minutes, and

2. the computation time of the tilted independent column approximation is of about 10-20 seconds, but the relative errors can be extremely large (they can reach values of 30% and even more).

The most important conclusion, that will be used further, is that the 3D-to-2D errors related to the calculation of the air-mass factor with an approximate two-dimensional radiative transfer model (in particular, the independent slice approximation) are below 4%. In other words, cloud effects can be analyzed by computing the air-mass factor in a two-dimensional geometry. The 3D-to-2D errors that we have to take into account are not large.

The retrieval algorithms proposed so far have more of a theoretical value. The reasons are the following.

1. The algorithms that can come into play, the tilted independent column approximation and the independent slice approximation, are either inaccurate (the first one), or require a rather long computation time (the second one).

2. Moreover, the independent slice approximation requires the knowledge of the cloud extinction field in a plane along the solar direction. In principle, cloud information can be obtained from co-located imagers, as for example, the Moderate Resolution Imaging Spectroradiometer (MODIS) on board the Terra and Aqua satellites, and the Visible Infrared Imaging Radiometer Suite (VIIRS) on board the Suomi National Polar-Orbiting Partnership spacecraft. The main cloud products delivered by MODIS/VIIRS are the cloud mask (indicator function of the cloud field), cloud optical thickness, cloud-top height (cloud-top pressure), and effective radius of the size distribution. In the MODIS/VIIRS retrieval algorithm, the cloud geometrical thickness is derived under the assumption that the clouds are homogeneous in the vertical direction, or equivalently, that the liquid water content does not change with the altitude. However, the main assumption of the MODIS/VIIRS retrieval algorithm is the independent column approximation, which cannot work hand in hand with a two-dimensional radiative transfer model (the inconsistency of the two models is obvious). Although, the cloud extinction field can be reconstructed by cloud tomography using multi-angle measurements [24-27], this task is beyond the goal of the project.

In this context, the retrieval algorithm that will be used in the project is the one proposed in Refs. [28] and [29]. This algorithm can be interpreted as a “surrogate cloud method”. Essentially, regardless of whether the scene is clear or cloudy, a surrogate cloud is introduced in the field of view of the instrument using as primary information the measured TOA reflectance. Because, the measured TOA radiance carries information about the three-dimensional effects, the surrogate cloud is intended to take these effects into account. The cloud properties are determined by a cloud retrieval algorithm, while the inverse model for retrieving the total column amount of NO_2 is the DOAS model. In DOAS, the air-mass factor is computed under the independent column approximation, which is the same assumption used by the cloud retrieval algorithms.

Considering that the cloud is a Lambertian reflecting surface with a fixed albedo $A_\mathrm{c} = 0.8$, the retrieval algorithm involves the following steps.

1. compute the cloud fraction c and the cloud top pressure p_c from the measured TOA reflectance R_mes using a cloud retrieval algorithm; schematically, we write

$$R_\mathrm{mes} \overset{\text{cloud retrieval algorithm}}{\longrightarrow} (c, p_\mathrm{c}); \tag{42}$$

2. compute the air-mass factor of a partly cloudy scene as

$$\mathrm{A}_\mathrm{1D}(X_{\mathrm{aNO}_2}) = (1-c)\mathrm{A}^\mathrm{clr}_\mathrm{1D}(X_{\mathrm{aNO}_2}, A_\mathrm{s}, p_\mathrm{s}) + c\mathrm{A}^\mathrm{cld}_\mathrm{1D}(X_{\mathrm{aNO}_2}, A_\mathrm{c}, p_\mathrm{c}), \tag{43}$$

where A_s and p_s are the surface albedo and the surface pressure, respectively, and $\mathrm{A}^\mathrm{clr}_\mathrm{1D}$ and $\mathrm{A}^\mathrm{cld}_\mathrm{1D}$ are the air-mass-factors for a cloud-free and a fully cloudy scene, respectively;

3. compute the slant column S_{NO_2} from the measured TOA reflectance R_mes using the DOAS equation; schematically, we write

$$R_\mathrm{mes} \overset{\text{DOAS}}{\longrightarrow} S_{\mathrm{NO}_2}; \tag{35}$$

4. compute the total column amount of NO_2 as

$$X_{\mathrm{NO}_2} = \frac{S_{\mathrm{NO}_2}}{\mathrm{A}_{1\mathrm{D}}(X_{\mathrm{aNO}_2})}. \tag{44}$$

Note that the air-mass-factors $\mathrm{A}_{1\mathrm{D}}^{\mathrm{clr}}$ and $\mathrm{A}_{1\mathrm{D}}^{\mathrm{cld}}$ are computed by a one-dimensional radiative transfer model for an assumed (a priori) total column X_{aNO_2}.

In a sensitivity study, the bias in the air-mass-factor can be computed by considering a two-dimensional box-cloud. This simplification is justified by the fact that the 3D-to-2D errors are not large, and so, that the cloud effects can be analyzed by computing the air-mass factor for a two-dimensional geometry. More precisely, the bias is calculated as

$$\Delta A(X_{\mathrm{aNO}_2}) = \mathrm{A}_{2\mathrm{D}}(X_{\mathrm{aNO}_2}) - \mathrm{A}_{1\mathrm{D}}(X_{\mathrm{aNO}_2}). \tag{45}$$

The air-mass-factor $\mathrm{A}_{1\mathrm{D}}$ is computed by means of Eqs. (42) and (43) with the measured TOA reflectance R_{mes} replaced by the TOA reflectance $R_{2\mathrm{D}}$, while the simulated TOA reflectance $R_{2\mathrm{D}}$, as well as, the air-mass factor $\mathrm{A}_{2\mathrm{D}}$ are computed by a two-dimensional radiative transfer model. In Ref. [28], the bias was parameterized as a function of the NO_2 profile height, the cloud top height of the neighboring pixel, the slant cloud optical thickness, and the cloud shadow fraction. In practice, the cloud information can be obtained from VIIRS, which uses the same independent column approximation as the retrieval algorithm.

2. Retrieval algorithms for 3D cloud effects based on synthetic and real spectra

2.1 The OCRA/ROCINN CAL and CRB treatments

The OCRA/ROCINN algorithm tandem allows the estimation of cloud macrophysical parameters from radiometric measurements in the UV/VIS/NIR, including cloud information about its coverage, altitude, and optical thickness/brightness.

OCRA (Optical Cloud Recognition Algorithm) infers the cloud fraction from UV/VIS reflectances by means of image analysis, under the assumption that the sensor measurements can be separated in two different components: the contribution due to the cloud-free background plus the contribution due to the presence of clouds. The difference between the expected sensor reflectances $\rho_{0,i}$ under cloud-free conditions and the actual sensor reflectances ρ_i is mapped into a radiometric cloud fraction f_C within the range [0, 1] by using a semiempirical formula depending on offset (β_i) and scaling (α_i) parameters. The cloud-free reflectance maps are created by data aggregation of measurements from a significant number of sensor datasets. For each map cell, the cloud-free reflectance is determined as the smallest reflectance value found in the complete time series, or as the farthest value from the white point if the reflectances are first translated into a normalised color space. To account for the time variations of the cloud-free reflectance at each map location, the cloud-free maps are created on a monthly basis. The offset and scaling parameters are estimated from the analysis of the histograms of differences ($\rho_i - \rho_{0,i}$) for a given dataset. A detailed explanation of the OCRA algorithm can be found in [30] and [31].

ROCINN (Retrieval Of Cloud Information using Neural Networks) infers two cloud macrophysical parameters from NIR measurements in the oxygen absorption bands. These cloud parameters are estimated by means of a regularised Gauss-Newton-like inversion process [14]. The fitted model is a weighted linear combination of two artificial neural networks: one that emulates a radiative transfer model under cloud-free conditions, weighted by the factor $(1 - f_C)$; and another one that emulates a radiative transfer model under presence of one cloud, weighted by the factor f_C. The weighting factors are computed using the cloud fraction f_C previously determined with the OCRA algorithm. ROCINN allows the use of two different types of cloud models in the retrieval process:

- **CRB** (Cloud as Reflective Boundaries), in which clouds are modelled as Lambertian surfaces, and for which the retrieved ROCINN parameters are the cloud-centroid height and cloud albedo; and
- **CAL** (Cloud As Layers), in which clouds are modelled as a homogeneous layer of scattering particles, and for which the retrieved ROCINN parameters are the cloud-top height and cloud optical thickness.

A more detailed explanation of the ROCINN algorithm can be found in [32] and [31]. The cloud parameters retrieved by ROCINN are a priori information used for the retrieval of trace gas columns of nitrogen dioxide, so the uncertainties in the cloud parameters due to the cloud model selection will be propagated to the results of the trace gas column retrievals. In particular, since both CRB and CAL models in ROCINN are based on a 1-dimensional atmosphere, the 3D cloud effects will not be taken into account by these models when simulating the top-of-atmosphere radiances that a sensor would measure.

2.2 Synthetic spectra NO_2 algorithms for 3D cloud effect treatment

The main retrieval algorithm for tropospheric NO_2 VCD retrieval from satellites is the differential optical absorption spectroscopy (DOAS) technique [11], which consists of two key steps: the slant column density (SCD) is retrieved by means of spectral fitting methods involving the direct solar spectra, the Earth-reflected solar spectra, and laboratory absorption cross sections of trace gases. The SCD corresponds to the integrated trace gas concentration along the light path taken by photons at the wavelength corresponding to the fitting window, as they travel from the Sun, through the atmosphere, and back to the satellite sensor. To convert the SCD into a vertical column density (VCD), one uses air mass factor (AMF) calculated with a radiative transfer model (RTM). The AMF is defined as the ratio of the atmospheric SCD and VCD. In clean regions, the error of the trace gas retrieval is dominated by the DOAS spectral fitting, while the uncertainty of the AMF becomes important for polluted regions. In general, AMFs depend on a number of factors, including surface albedo, cloud and aerosol properties, and the a priori profile shape of the measured trace gas.

Clouds have a strong influence on the retrieval of the trace gases. Since the UV-Vis sensors have a relatively coarse spatial resolution, ranging from a few kilometers to several tens of kilometers, only a small percentage of the observed pixels (10%–20%) are cloud-free [33], and most pixels are either fully or partly cloudy. Thus, trace gas retrieval algorithms rely on cloud property information provided for each ground pixel. Such information is important, since clouds have a significant impact on the photon path. The effect of clouds on the trace gas retrieval has been studied by several authors (e.g. [34], [35], [36]). In these studies, the cloud treatment is based on the independent pixel approximation (IPA). A simple cloud correction scheme is generally used, which treats clouds as Lambertian surfaces or scattering layers and relies on the concepts of cloud fraction, cloud top albedo/cloud optical thickness, and cloud top pressure [37] [38] [39]. These approaches are based on the determination of the mean photon path in the visible and/or near-infrared (NIR) bands from analysis of a spectral feature of a well-mixed species.

In this study, several approaches are tested to correct the presence of clouds in the NO_2 retrievals:

1. The Fast Retrieval Scheme for Clouds from the Oxygen A band (**FRESCO**) algorithm, developed by the Royal Netherlands Meteorological Institute (KNMI), models the effective cloud fraction and cloud pressure (height) using the O_2 A-band centered at 760nm [39] [40]. The cloud parameters are retrieved from top-of-atmosphere reflectances in three 1-nm wide wavelength windows at 758-759nm (no absorption), 760-761nm (strong absorption), and 765-766nm (moderate absorption). FRESCO uses a Lambertian cloud model, where the cloud is assumed to be a Lambertian reflector with a fixed albedo of 0.8.
2. The **O_2-O_2** algorithm has been developed by KNMI and was initially developed for OMI because this instrument does not cover the spectral range of the O_2 A-band at 760 nm [41] [42]. The algorithm uses satellite measurements from the O_2-O_2 (O_4) absorption window at 477 nm to retrieve the effective cloud fraction and the cloud height using a similar cloud model as the one used in FRESCO. However, it is more sensitive to clouds at lower altitudes and to aerosols because it uses O_2-O_2 collision-induced absorption. As in FRESCO, a fixed cloud albedo of 0.8 is assumed.
3. The **OCRA/ROCINN** algorithm: the operational TROPOMI cloud product was developed by DLR as a two-step algorithm. First, OCRA, an algorithm for cloud detection by optical sensors, is applied to TROPOMI measurements in the UV-Vis spectral region to retrieve the cloud fraction a priori. Using the colour-space approach, the UV-Vis reflectances of the observed scene are translated to colours to obtain the radiometric cloud fraction. Second, the OCRA a priori cloud fraction and NIR TROPOMI measurements are taken as input to a machine learning algorithm, ROCINN, to retrieve the cloud-top height, the cloud optical thickness, and the cloud albedo from reflectivity measurements in and around the O_2 A-band between 758 and 771 nm. Two cloud models are implemented in ROCINN: the Clouds-As-Layers (CAL) model and the Clouds-as-Reflecting-Boundaries (CRB) model. ROCINN CAL treats clouds as homogeneous layers of scattering liquid water particles to retrieve cloud fraction, cloud top height, and

cloud optical thickness. The cloud base height from ROCINN CAL is not a retrieved quantity; instead, the cloud is assumed to have a constant geometrical thickness of 1 km. In ROCINN CRB, clouds are Lambertian-equivalent reflectors, with cloud fraction, cloud height, and cloud top albedo as output. Cloud fractions that are smaller than 0.05 in OCRA a priori are set to zero in the ROCINN CAL and CRB cloud fractions, and the ROCINN retrieval is not triggered under these “clear-sky” conditions.

4. The "**surrogate cloud method**" is a technique designed to enhance measurements by introducing a hypothetical cloud into the field of view of an observational instrument, regardless of actual weather conditions being clear or cloudy. This method primarily utilizes the measured top-of-atmosphere (TOA) reflectance to infer the presence of this surrogate cloud. The rationale behind this approach is that TOA radiance captures intricate three-dimensional effects of the atmosphere, which are crucial for accurate data interpretation. To account for 3D effects, the surrogate cloud is used to simulate the impact of real clouds on the radiance observed by the instrument. The properties of the surrogate cloud are meticulously determined using a cloud retrieval algorithm that extracts detailed cloud characteristics from the observed data.

2.3 S5P/TROPOMI NO_2 algorithms for 3D cloud effect treatment

In this study, tropospheric NO_2 retrievals from TROPOMI measurements are based on a DLR research NO_2 retrieval algorithm described in Liu et al. (2021) with application of improved ancillary input datasets. Independent from the operational processing, the DLR NO_2 retrieval algorithm is flexible and versatile, capable of accommodating new settings and input datasets for total and tropospheric NO_2 retrieval, thereby investigating the influence of different cloud models on tropospheric NO_2 retrievals.

Overall, DLR NO_2 retrieval algorithm for the TROPOMI instrument consists of three steps: (1) the spectral retrieval of total NO_2 slant columns using the differential optical absorption spectroscopy (DOAS) method, (2) the separation of slant columns into stratospheric and tropospheric contributions, and (3) the conversion of tropospheric slant columns to tropospheric vertical columns using air mass factor (AMF) calculation. Table 3 summarizes the DLR TROPOMI NO_2 retrieval algorithm attributes, parameters for spectral fitting and AMF calculations used in this study. For the calculation of NO_2 slant columns, a fitting window of 405-465 nm is applied in the DOAS fit. Absorption cross-sections of interfering species and a linear intensity offset correction are applied. The stratospheric NO_2 column is estimated using a directionally dependent STRatospheric Estimation Algorithm from Mainz (DSTREAM) [43], which accounts for the dependency of the stratospheric NO_2 on the viewing geometry. In the tropospheric AMF calculation, the surface albedo is based on the TROPOMI directionally dependent Lambertian-equivalent reflectivity (DLER) v2.0 climatology, which is the latest version of TROPOMI surface LER climatology database based on 5 years of TROPOMI version 2.1 reprocessed level-1b data [44]. To account for the varying sensitivity of NO_2 at different altitudes, the CAMS global forecast a priori NO_2 profiles are used in this algorithm. Compared to the TM5-MP a priori NO_2 profiles with a spatial resolution of 1°×1° and 34 vertical levels used in the current operational TROPOMI NO_2 retrieval, the improved spatial resolution (0.4°×0.4°, 137 levels) as well as more up-to-date chemistry and emissions for trace gas species in the CAMS forecast model enhance the capability to capture the local NO_2 distribution accurately, especially in regions with large heterogeneity and variability.

Table 3. Summary of DLR TROPOMI tropospheric NO_2 retrieval algorithm attributes, parameters for spectral fittings, and parameters for AMF calculations.

Spectral fit settings for slant column retrievals	Fitting window	405 – 465 nm
	Absorption cross sections	NO_2 at 220 K, O_3 at 228 K, H_2O_{vap} at 293 K, O_4 at 293 K, H_2O_{liq} at 297 K

	Ring effect	Ring reference spectrum as a pseudo absorber
	Polynomial	5th orders
	Offset	A linear intensity offset correction
	Destriping correction	A posteriori box-car averaging method using the daily averaged cross-track variability of NO_2 slant columns over clean reference sectors between 20 °S and 20 °N
Stratospheric correction	DSTREAM	
Ancillary input parameters for AMF calculations	Cloud parameter	(1) OCRA/ROCINN_CRB version 2.4 (2) OCRA/ROCINN_CAL version 2.4 (3) OCRA/ROCINN_surrogate CAL version 2.4
	Surface albedo	TROPOMI DLER v2.0 climatology
	A priori NO_2 profile	CAMS global atmospheric composition forecasts (0.4°x0.4°, 137 levels)

The retrieval of tropospheric NO_2 is influenced by the cloud parameters, which derives variations in scene albedo and the photon path redistribution in the troposphere. Given the high computational intensity of multi-dimensional radiative transfer models, the practical application in remote sensing often leans towards the use of one-dimensional models. Therefore, the independent pixel approximation (IPA) is employed as a solution for horizontally inhomogeneous cloud scenes. IPA treats each pixel independently by extending the atmospheric column associated with that pixel into a horizontally infinite (one-dimensional) atmosphere characterized by horizontally homogeneity. As a result, a one-dimensional problem is solved for each pixel. IPA performs plane-parallel calculations by giving weights depending on the probability distributions of the cloud properties. For example, if a pixel is partially covered by the cloud, the cloud fraction is introduced, which shows the ratio of the pixel area containing cloud to the total pixel area. The final radiance is derived as a weighted sum of one-dimensional solutions. In the tropospheric NO_2 retrieval, the AMF calculation adopts the IPA to account for cloud-contaminated pixels, which expresses the AMF as a linear combination of a cloudy AMF (M_{cld}) and a clear-sky AMF (M_{clr}):

$$M = \omega M_{cld} + (1 - \omega) M_{clr} \qquad (46)$$

with ω the radiance weighted cloud fraction derived from the effective cloud fraction (c_f):

$$\omega = \frac{c_f I_{cld}}{(1 - c_f) I_{clr} + c_f I_{cld}} \qquad (47)$$

where I_{cld} and I_{clr} representing the radiances from the cloudy and clear parts of the pixel, respectively. The values of I_{cld} and I_{clr} depends on TROPOMI viewing geometries, surface albedo and assumed cloud albedo.

In this study, we evaluate the 3D cloud effect treatment on the tropospheric NO_2 retrieval using three different cloud model datasets: (1) OCRA/ROCINN CRB v2.4, (2) OCRA/ROCINN CAL v2.4, and (3) OCRA/ROCINN surrogate CAL v2.4. OCRA, an algorithm for cloud detection by optical sensors, is applied to TROPOMI measurements in the UV-Vis spectral range to retrieve the cloud fraction a priori]. The OCRA a priori cloud fraction and NIR TROPOMI measurements are taken as input to a machine learning algorithm, ROCINN, to retrieve the cloud-top-height, the cloud optical thickness, and the cloud albedo from reflectivity. Here, two cloud models are implemented in ROCINN: the Clouds-As-Layers (CAL) model and the Clouds-as-Reflecting-Boundaries (CRB) model. The operational TROPOMI cloud product OCRA/ROCINN CRB and CAL are described in more detailed in Sect. 2.1.

Here, to account for 3D cloud effects more accurately, we employ a pixel-specific online AMF calculation instead of using a pre-calculated altitude-dependent AMF look-up table (LUT). Compared to the AMF

calculation through linear interpolation from the altitude-dependent AMF LUT, pixel-specific online calculations can derive more precise AMF estimates by using original viewing geometries and input ancillary parameter values, including cloud heights (pressure), radiance weighted cloud fractions, surface pressure and albedo.

The CRB-based cloud retrieval generally indicates a cloud height (pressure) close to the middle altitude, as CRB neglects the oxygen absorption within a cloud layer, leading to misinterpretation of the smaller top-of-atmosphere reflectance as a lower cloud layer. Compared to the CRB-based cloud correction, the use of the CAL model describes more realistically the process of radiative transfer in the atmosphere, particularly in regions below clouds. The CAL model treats clouds as optically uniform layers of light-scattering water droplets, and thereby scattering events are described by the single scattering phase functions, whereas the single scattering phase functions of water droplets are not used in the CRB model. Consequently, the CAL model better represents real situations by reflecting sensitivities both within and below the cloud layers.

In the CAL model, a one-dimensional cloud is characterized by its cloud fraction, cloud top height, and cloud optical thickness. The a priori cloud fraction obtained from OCRA does not require radiative transfer simulations and relies solely on reflectance measurements. Therefore, a feasible concept of a surrogate cloud model can be implemented in OCRA as the retrieved cloud fraction includes information from surrounding pixels. This surrogate cloud model, implemented in the OCRA/ROCINN CAL processor, accounts for 3D cloud effects by reflecting cloud shadow effects. Figure 16 shows an example of TROPOMI radiance weighted cloud fractions with the CAL model treatment (Figure 16a) and the surrogate CAL model treatment (Figure 16b). The effect of surrogate cloud model is more pronounced at the cloud edges (Figure 16c). Hence for cloudy free pixels, the cloud should be artificially added. One way to that is to apply smoothing to the cloud fraction field with a Gaussian kernel. Literature [26, 45, 46, 47] suggests using smoothing kernels with a width of approximately 5-10 kilometers, corresponding to 1-2 pixels of the TROPOMI satellite sensor. The NO_2 retrieval within the surrogate cloud model using DOAS approach is based on the independent pixel approximation. As the cloud fraction map provided by OCRA is radiometric (i.e. it uses real three-dimensional radiance field), it can be regarded as surrogate as well.

In the NO_2 map on March 3, 2021, Figure 17, we observe variations in NO_2 concentrations across three different data sets: the original retrieval, and two alternative retrievals where the cloud fraction data has been convolved using Gaussian kernels of differing widths (3 km and 7 km). As anticipated, the differences in retrieved NO_2 levels are particularly pronounced in regions characterized by significant pollution and where there exists strong spatial variability in cloud coverage.

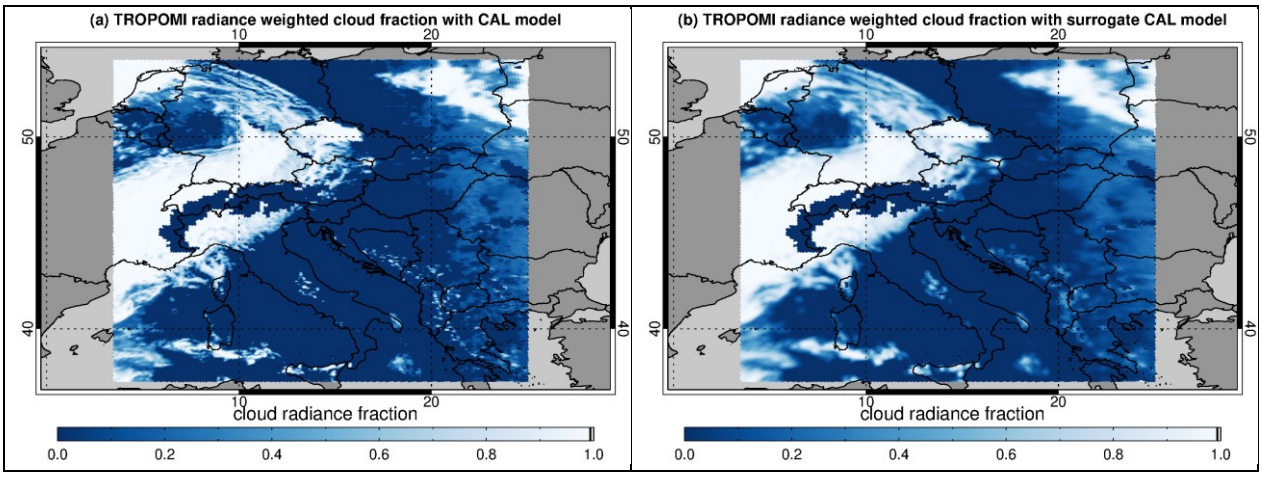

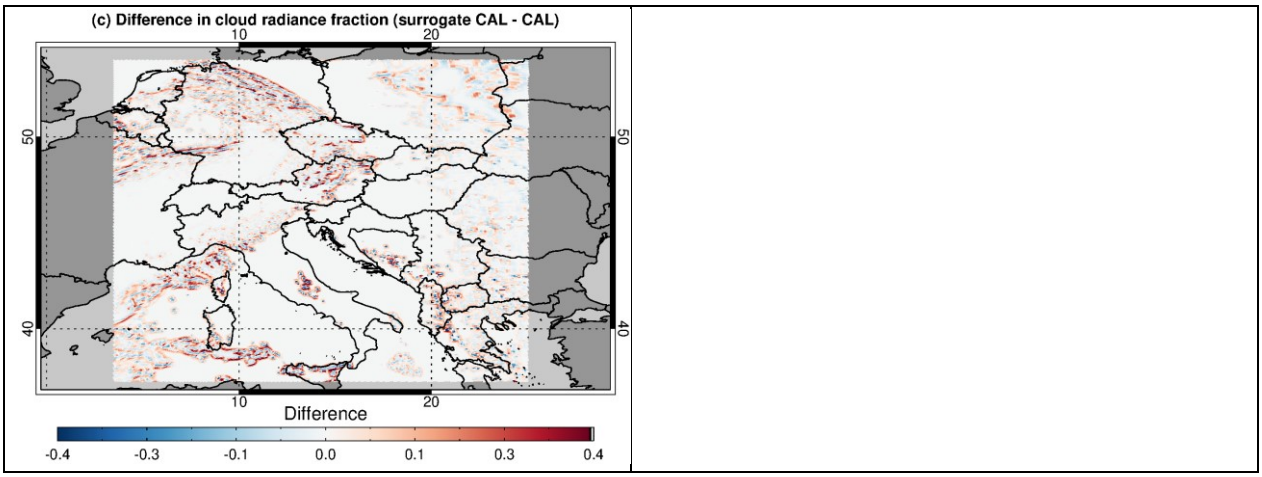

Figure 16. Maps of TROPOMI radiance weighted cloud fractions from (a) the OCRA/ROCINN CAL model, and (b) the OCRA/ROCINN surrogate CAL model for 3 March 2021 over Europe. (c) Differences in radiance weighted cloud fractions (surrogate CAL – CAL; b-a in this figure) for the corresponding scene.

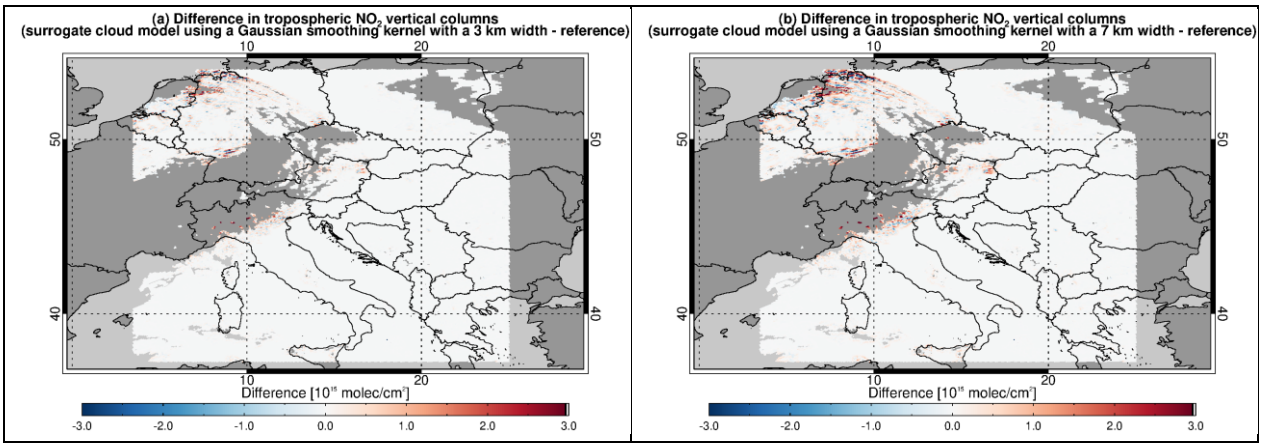

Figure 17. Difference in retrieved tropospheric NO_2 column values when using the original OCRA cloud fraction data versus cases where the cloud fraction data has been smoothed using a Gaussian smoothing kernel with (a) a width of 3 km and (b) a kernel width of 7 km.

3. Conclusions

From the *theoretical treatise* on the different methodologies to treat cloudy pixels, an inherent risk in remote sensing observations of the atmosphere, the following main points can be extracted. With respect to the numerical analysis related to the computation of the air-mass factor has shown that the relative errors of the independent slice approximation are below 4%, while the computation time is around 1-3 minutes, and that the computation time of the tilted independent column approximation is of about 10-20 seconds, but the relative errors can be extremely large (they can reach values of 30% and even more). With respect to the retrieval of the total column amount of NO_2 under cloudy conditions led to the following conclusions:
1. The three-dimensional radiative transfer model yields the highest accuracy (relative errors smaller than 0.05%). However, the extremely high computation time of about 14 hours disqualifies this method for processing a large amount of data.
2. The independent slice approximation with a computation time of 6-8 minutes and relative errors below 5% is a well-balanced compromise between accuracy and efficiency.
3. The nonlocal independent slice approximation and a zeroth-order stochastic model yield relative errors of about 3-4%. However, the small accuracy improvement as compared to the independent splice approximation does not justify the high computation times of 25-40 minutes.
4. The tilted independent column approximation with a computational time of 20-30 seconds can lead to large relative errors (of about 20%). Therefore, from the point of view of accuracy, the method is not recommended.
The most important conclusion, led to the application of the surrogate cloud methodology being applied to both synthetic and real observations of the NO_2 atmospheric content, is that the 3D-to-2D errors related to the calculation of the air-mass factor with an approximate two-dimensional radiative transfer model (in particular, the independent slice approximation) are below 4%. In other words, cloud effects can be analyzed by computing the air-mass factor in a two-dimensional geometry.

For the *application of different 3D cloud treatments on synthetic spectra*: several cloud correction methods (FRESCO, O2-O2, OCRA/ROCINN) implemented in operational trace gas products using a series of synthetic data. These approaches mitigate the effects of clouds in NO_2 retrievals, particularly for SZA below 60°. However, existing techniques are insufficient for correcting the cloud shadowing effects, resulting in notable positive biases in the calculation of the AMF.

For the *application of different 3D cloud treatments on real spectra*: the 3D cloud effect treatments on S5P/TROPOMI tropospheric NO_2 retrieval using three different cloud products (OCRA/ROCINN CRB, OCRA/ROCINN CAL, and OCRA/ROCINN surrogate CAL) were investigated. The surrogate cloud model was implemented using Gaussian kernels of different widths to convolve cloud fraction data, thereby accounting for 3D cloud shadow effects. The findings highlighted distinct variations in tropospheric NO_2 levels, especially in heavily polluted areas with significant spatial variability in cloud coverage such as cloud boundaries. The minimal impact observed from the smoothing could be attributed to the nature of the cloud fraction field provided by OCRA. Specifically, the OCRA utilizes radiometric radiances, which are influenced by 3D effects. Consequently, the retrieved cloud fraction corresponds to the surrogate cloud model. It is important to note that the analysis of the influence of smoothing kernels, as discussed in [45], was primarily based on synthetic cloud fractions. In this context, the effect of smoothing was more pronounced.

References

[1] Evans, K.F. The spherical harmonic discrete ordinate method for three-dimensional atmospheric radiative transfer. J. Atmos. Sci. 1998, 55, 429-446. DOI:10.1175/1520-0469(1998)055<0429:TSHDOM>2.0.CO;2

[2] Gabriel, P. M.; Evans, K.F. Simple radiative transfer methods for calculating domain-averaged solar fluxes in in- homogeneous clouds. J. Atmos. Sci. 1996, 53, 858–877.

[3] Varnai, T.; Davies, R. Effects of cloud heterogeneities on shortwave radiation: Comparison of cloud-top variability and internal heterogeneity. J. Atmos. Sci. 1999, 56, 4206–4224.

[4] Marshak, A. M.; Davis, A.B.; Wiscombe, W.; Cahalan, R. Radiative smoothing in fractal clouds. J. Geophys. Res. 1995, 100, 26 247– 26 261.

[5] Zuidema, P.; Evans, K.F. On the validity of the independent pixel approximation for boundary layer clouds ob- served during ASTEX. J. Geophys. Res. 1998, 103, 6059–6074.

[6] Wissmeier, U.; Buras-Schnell, R.; Bernhard, M. PaNTICA: A fast 3D radiative transfer scheme to calculate surface solar irradiance for NWP and LES models. Journal of Applied Meteorology and Climatology 2013, 52, 1698-1715. 10.1175/JAMC-D-12-0227.1.

[7] Doicu, A.; Efremenko, D.S.; Loyola, D.; Trautmann, T. Discrete ordinate method with matrix exponential for stochastic radiative transfer in broken clouds. J. Quant. Spectrosc. Radiat. Transf. 2014, 138, 1-16.

[8] Stephens, G.L. Radiative transfer through arbitrarily shaped optical media. Part II: Group theory and simple closures. J. Atmos. Sci. 1988, 45, 1818–1848.

[9] Doicu, A.; Efremenko, D.S. Assesstment of 3D cloud inhomogenieties on NO_2 retrieval [in preparation]

[10] Doicu, A.; Efremenko, D.S.; Trautmann, T. A Proof-of-Concept Algorithm for the Retrieval of Total Column Amount of Trace Gases in a Multi-Dimensional Atmosphere. Remote Sens. 2021, 13, 270. https://doi.org/10.3390/rs13020270

[11] Platt, U.; Stutz, J. Differential optical absorption spectroscopy. Principles and Applications. Springer-Verlag: Berlin, Heidelberg, 2008.

[12] Doicu A, Efremenko DS. Linearizations of the spherical harmonic discrete ordinate method (SHDOM). Atmosphere 2019, 10, 292; doi:10.3390/atmos10060292

[13] Doicu A. Efremenko D, Trautmann T. A Spectral Acceleration Approach for the Spherical Harmonics Discrete Ordinate Method. Remote Sens., 12, 3703.

[14] Doicu, A.; Trautmann, T.; Schreier, F. Numerical Regularization for Atmospheric Inverse Problems. Springer-Verlag, Berlin Heidelberg, 2010.

[15] Alexandrov, M.D., A. Marshak , and A.S. Ackerman. Cellular statistical models of broken cloud fields. Part I: Theory . J. Atmos. Sci. 2010, 67, 2125-2151, https://doi.org/10.1175/2010JAS3364.1.

[16] Liu S. Inversion models for the retrieval of total and tropospheric NO2 columns. Atmosphere 2019, 10, 607; doi:10.3390/atmos10100607.

[17] Rozanov VV, Rozanov AV. Differential optical absorption spectroscopy (DOAS) and air mass factor concept for a multiply scattering vertically inhomogeneous medium: theoretical consideration. Atmos. Meas. Tech., 2010, 3, 751–780.

[18] Rozanov VV, Vountas M. Radiative transfer equation accounting for rotational Raman scattering and its solution by the discrete-ordinates method. J Quant Spectrosc Radiat Transfer. 2010, 133,603-618.

[19] Anderson, G.; Clough, S.; Kneizys, F.; Chetwynd, J.; Shettle, E. AFGL atmospheric constituent profiles (0-120 km). Tech. Rep. AFGL- TR-86-0110, Air Force Geophys. Lab., Hanscom Air Force Base, Bedford, Mass., 1986.

[20] Bodhaine, B. A.; Wood, N. B.; Dutton, E. G.; Slusser, J. R. On Rayleigh optical depth calculations. J. Atm. Ocean Technol. 1999, 16, 1854–1861.

[21] Vandaele, A.; Hermans, C.; Simon, P.; Carleer, M.; Colin, R.; Fally, S.; Merienne, M.; Jenouvrier, A.; Coquart, B. Measurements of the NO2 absorption cross-section from 42000 cm-1 to 10 000 cm-1 (238–1000 nm) at 220 K and 294 K. J. Quant. Spectrosc. Radiat. Transfer 1998, 59, 171-184.

[22] Serdyuchenko, A.; Gorshelev, V.; Weber, M.; Chehade, W.; Burrows, J.P. High spectral resolution ozone absorption cross-sections – Part 2: Temperature dependence. Atmos. Meas. Tech. 2014, 7, 625–636.
[23] Thalman, R.; Volkamer, R. Temperature Dependent Absorption Cross-Sections of O2-O2 collision pairs between 340 and 630 nm at atmospherically relevant pressure. Phys. Chem. Chem. Phys. 2013. Doi:10.1039/C3CP50968K.
[24] A. Levis, Y. Y. Schechner, A. Aides and A. B. Davis, " Airborne Three-Dimensional Cloud Tomography," 2015 IEEE International Conference on Computer Vision (ICCV), Santiago, 2015, 3379-3387, doi: 10.1109/ICCV.2015.386.
[25] Boehm, C; Sourdeval, O.; Muelmenstadt, J.; Quaas, J.; Crewell, S. Cloud base height retrieval from multi-angle satellite data. Atmospheric Measurement Techniques. 2019, 12, 1841-1860.
[26] Doicu A, Efremenko D, Trautmann T. Cloud tomographic retrieval algorithms. I: Surrogate minimization method. J Quant Spectrosc Radiat Transfer. 2022, 277, 107954. https://doi.org/10.1016/j.jqsrt.2021.107954.
[27] Doicu A, Efremenko D, Trautmann T. Cloud tomographic retrieval algorithms. II: Adjoint method. J Quant Spectrosc Radiat Transfer. 2022, 285, 108177. https://doi.org/10.1016/j.jqsrt.2022.108177.
[28] Yu, H., Emde, C., Kylling, A., Veihelmann, B., Mayer, B., Stebel, K., and Van Roozendael, M.: Impact of 3D cloud structures on the atmospheric trace gas products from UV–Vis sounders – Part 2: Impact on NO_2 retrieval and mitigation strategies, Atmos. Meas. Tech., 2022, 15, 5743–5768, https://doi.org/10.5194/amt-15-5743-2022.
[29] Emde, C., Yu, H., Kylling, A., van Roozendael, M., Stebel, K., Veihelmann, B., and Mayer, B.: Impact of 3D cloud structures on the atmospheric trace gas products from UV–Vis sounders – Part 1: Synthetic dataset for validation of trace gas retrieval algorithms, Atmos. Meas. Tech. 2022, 15, 1587–1608, https://doi.org/10.5194/amt-15-1587-2022.
[30] Lutz, R.; Loyola, D.; Gimeno García, S.and Romahn, F. (2016) *OCRA radiometric cloud fractions for GOME-2 on MetOp-A/B*, Atmospheric Measurement Techniques, 9, 2357–2379.
https://doi.org/10.5194/amt-9-2357-2016
[31] Molina García, V. (2022) *Retrieval of cloud properties from EPIC/DSCOVR*. Doctoral thesis, Technical University of Munich, Germany.
https://mediatum.ub.tum.de/1662361
[32] Loyola, D.G.; Gimeno García, S.; Lutz, R.; Argyrouli, A.; Romahn, F.; Spurr, R.J.D.; Pedergnana, M.; Doicu, A.; Molina García, V.; and Schüssler, O. (2018) *The operational cloud retrieval algorithms from TROPOMI on board Sentinel-5 Precursor*, Atmospheric Measurement Techniques, 11, 409–427.
https://doi.org/10.5194/amt-11-409-2018
[33] Krijger, J. M., van Weele, M., Aben, I., and Frey, R.: Technical Note: The effect of sensor resolution on the number of cloud-free observations from space, Atmos. Chem. Phys., 7, 2881–2891, https://doi.org/10.5194/acp-7-2881-2007, 2007.
[34] Boersma, K. F., Eskes, H. J., and Brinksma, E. J.: Error analysis for tropospheric NO2 retrieval from space, J. Geophys. Res., 109, D04311, https://doi.org/10.1029/2003JD003962, 2004.
[35] Lorente, A., Folkert Boersma, K., Yu, H., Dörner, S., Hilboll, A., Richter, A., Liu, M., Lamsal, L. N., Barkley, M., De Smedt, I., Van Roozendael, M., Wang, Y., Wagner, T., Beirle, S., Lin, J.-T., Krotkov, N., Stammes, P., Wang, P., Eskes, H. J., and Krol, M.: Structural uncertainty in air mass factor calculation for NO_2 and HCHO satellite retrievals, Atmos. Meas. Tech., 10, 759–782, https://doi.org/10.5194/amt-10-759-2017, 2017.
[36] Liu, S., Valks, P., Pinardi, G., Xu, J., Argyrouli, A., Lutz, R., Tilstra, L. G., Huijnen, V., Hendrick, F., and Van Roozendael, M.: An improved air mass factor calculation for nitrogen dioxide measurements from the Global Ozone Monitoring Experiment-2 (GOME-2), Atmos. Meas. Tech., 13, 755–787, https://doi.org/10.5194/amt-13-755-2020, 2020.
[37] Loyola, D. G., Gimeno García, S., Lutz, R., Argyrouli, A., Romahn, F., Spurr, R. J. D., Pedergnana, M., Doicu, A., Molina García, V., and Schüssler, O.: The operational cloud retrieval algorithms from TROPOMI

on board Sentinel-5 Precursor, Atmos. Meas. Tech., 11, 409–427, https://doi.org/10.5194/amt-11-409-2018, 2018.
[38] Acarreta, J. R., De Haan, J. F., and Stammes, P.: Cloud pressure retrieval using the O2-O2 absorption band at 477 nm, J. Geophys. Res.-Atmos., 109, D05204, https://doi.org/10.1029/2003JD003915, 2004.
[39] Wang, P., Stammes, P., van der A, R., Pinardi, G., and van Roozendael, M.: FRESCOC: an improved O2 A-band cloud retrieval algorithm for tropospheric trace gas retrievals, Atmos. Chem. Phys., 8, 6565–6576, https://doi.org/10.5194/acp-8-6565-2008, 2008.
[40] Koelemeijer, R. B. A., Stammes, P., Hovenier, J. W., and de Haan, J. F.: A fast method for retrieval of cloud parameters using oxygen A band measurements from the Global Ozone Monitoring Experiment, J. Geophys. Res., 106, 3475–3490, 2001.
[41] Acarreta, J. R., De Haan, J. F., and Stammes, P.: Cloud pressure retrieval using the O2-O2 absorption band at 477 nm, J. Geophys. Res.-Atmos., 109, D05204, https://doi.org/10.1029/2003JD003915, 2004.
[42] Veefkind, J. P., de Haan, J. F., Sneep, M., and Levelt, P. F.: Improvements to the OMI O_2-O_2 operational cloud algorithm and comparisons with ground-based radar–lidar observations, Atmos. Meas. Tech., 9, 6035–6049, https://doi.org/10.5194/amt-9-6035-2016, 2016.
[43] Beirle, S., Hörmann, C., Jöckel, P., Liu, S., Penning de Vries, M., Pozzer, A., Sihler, H., Valks, P., and Wagner, T.: The STRatospheric Estimation Algorithm from Mainz (STREAM): estimating stratospheric NO2 from nadir-viewing satellites by weighted convolution, Atmos. Meas. Tech., 9, 2753–2779, https://doi.org/10.5194/amt-9-2753-2016, 2016.
[44] Tilstra, L. G., de Graaf, M., Trees, V. J. H., Litvinov, P., Dubovik, O., and Stammes, P.: A directional surface reflectance climatology determined from TROPOMI observations, Atmos. Meas. Tech., 17, 2235–2256, https://doi.org/10.5194/amt-17-2235-2024, 2024.
[45] Marshak, A. M.; Davis, A.B.; Wiscombe, W.; Cahalan, R. Radiative smoothing in fractal clouds. J. Geophys. Res. 1995, 100, 26 247– 26 261.
[46] Zuidema, P.; Evans, K.F. On the validity of the independent pixel approximation for boundary layer clouds observed during ASTEX. J. Geophys. Res. 1998, 103, 6059–6074.
[47] Wissmeier, U.; Buras-Schnell, R.; Bernhard, M. PaNTICA: A fast 3D radiative transfer scheme to calculate surface solar irradiance for NWP and LES models. Journal of Applied Meteorology and Climatology 2013, 52, 1698-1715. 10.1175/JAMC-D-12-0227.1.